Studies on Sintering Silicon Carbide-Nanostructured Ferritic Alloy Composites for Nuclear Applications

Zhihao Hu

Thesis submitted to the faculty of
Virginia Polytechnic Institute and State University
in partial fulfillment of the requirements for the degree of

Master of Science
in
Materials Science and Engineering

Kathy Lu, Chair
Alex O. Aning
David E. Clark

June 29, 2016
Blacksburg, VA

Keywords: nanostructured ferritic alloy (NFA), silicon carbide (SiC), spark plasma sintering (SPS), density, microstructure, hardness

Studies on Sintering Silicon Carbide-Nanostructured Ferritic Alloy Composites for Nuclear Applications

Zhihao Hu

ABSTRACT

Nanostructured ferritic alloy and silicon carbide composite materials (NFA–SiC) were sintered with spark plasma sintering (SPS) method and systematically investigated through X-ray diffraction (XRD), scanning electron microscopy (SEM), as well as density and Vickers hardness tests. Pure NFA, pure SiC, and their composites NFA–SiC with different compositions (2.5 vol% NFA–97.5 vol% SiC, 5 vol% NFA–95 vol% SiC, 97.5 vol% NFA–2.5 vol% SiC, and 95 vol% NFA–5 vol% SiC) were successfully sintered through SPS.

In the high-NFA samples, pure NFA and NFA–SiC, minor γ-Fe phase formation from the main α-Fe matrix occurred in pure NFA 950 °C and 1000 °C. The densities of the pure NFA and NFA–SiC composites increased with sintering temperature but decreased with SiC content. The Vickers hardness of the pure NFA and NFA–SiC composites was related to density and phase composition. In the high-SiC samples, NFA addition of 2.5 vol% can achieve full densification for the NFA–SiC samples at relative low temperatures. With the increase in sintering temperature, the Vickers hardness of the pure SiC and NFA–SiC composite samples were enhanced. However, the NFA–SiC composites had relative lower hardness than the pure SiC samples. A carbon layer was introduced in the NFA particles to prevent the reaction between NFA and SiC. Results indicated that the carbon layer was effective up to 1050 °C sintering temperature. Green samples of gradient-structured NFA–SiC composites were successfully fabricated through slip casting of an NFA–SiC co-suspension.

Acknowledgements

I greatly appreciate my advisor, Prof. Dr. Kathy Lu, who contributes her carefully guidance and warmly assistance and enormous supports to my academic research during the past three years. Thanks to cultivation for my academic and professional skills, I can complete my research target and obtain my master degree.

I would like to thank Dr. Thomas Staley, and Dr. Carlos Suchicital for the guidance of my laboratory works. Thanks a lot to my committee members, Dr. Alex Aning, and Dr. David Clark for their hard work and helpful advice, not only in the research, but also in the life. I would also like to thank my colleagues, Donnie Erb, Hongfei Ju, Michelle Gervasio, Kris Shen, Hesham Elmkharram, Dr. Zhi Tang, and Dr. Kaijie Ning for their useful discussions and laboratory supports. I would also like to thank the entire Materials Science and Engineering department staff for their administrative support. I am also indebted to Steve McCartney who works in the institute of Nanoscale Characterization and Fabrication Laboratory for the assistance in using the SEM, and Jay Tuggle for assistance in using the Triboindenter. Last, but not least, I would like to thank my friends and family for their support, patience, and confidence.

I would like to sincerely thank the Office of Nuclear Energy of Department of Energy for providing financial support for this work under grant number #DE-NE0008264.

Table of Contents

List of Figures

List of Tables

1 Introduction

1.1 Silicon carbide

Silicon carbide (SiC) possesses high strength and chemical stability even at very high temperatures; thus, SiC is a useful engineering ceramic material[4]. When exposed to radiation, SiC materials have low induced activation and low after-heat properties. SiC materials also present unique and exceptional stability when exposed to high radiation[5, 6, 7]. These properties make SiC an attractive candidate for application in harsh radiation environments. The thermal diffusion of dopants in SiC requires extremely high temperatures because the impurities in SiC have extremely low diffusivities; this condition is different from that in traditional semiconductor materials. SiC is also utilized as a fission product barrier because of its low diffusivity for impurities in tristructural–isotropic fuel[8]. In addition, this low diffusivity of fission products has been demonstrated at temperatures exceeding 2000 K[9, 10]. As a result, SiC-based ceramic composites have been considered potential and attractive structural materials for fission energy systems for decades.

SiC is a highly covalent bonded compound[11]. Therefore, SiC is difficult to densify without sintering additives. This difficulty limits the nuclear applications of SiC. Sintering additives, which generally include boron, yttrium oxide, and aluminum oxide, are utilized to promote SiC densification[12, 13]. However, their addition might be detrimental to irradiation performance, such as neutron absorption, and could thus cause swelling[14]. Sintering additives also introduce some liquid phase at grain boundaries[15]. They usually reduce the decomposition temperature of SiC and impede the mechanical properties[13, 16, 17]. To achieve full density for SiC while avoiding these drawbacks, no sintering additives were used in the present study, and a non-conventional sintering process called spark plasma sintering (SPS) was adopted. SPS relies on pulsed direct current (DC) passing through an electrical pressure-conducting die containing a green sample[15, 18]. In-situ uniaxial pressure is applied during sintering. The main benefit is that full density can be easily reached easily, and the entire process requires only a few minutes, thus minimizing grain growth[14, 18].

Sintering of dense materials requires two key requirements, namely, achieving full density and maintaining the grain size. While maintaining the grain size can be easily realized by limiting the sintering temperature and time, achieving full density requires a more careful consideration of sintering driving forces. A number of techniques, such as two-step sintering, high-pressure assisted sintering, and SPS, have been successful utilized. SPS is realized by subjecting the green compact to arc discharges generated by a pulsed electric current and

simultaneous pressure. It possesses better characteristics when compared with conventional pressure-assisted sintering processes probably because of the effects of spark plasma, spark impact pressure, Joule heating, electromagnetic field, electromigration, surface current, and rapid heating. The externally applied pressure is generally 30–200 MPa. The heating rate is 100–1000 °C·min^{-1}, which is much faster than that of electric resistance rapid heating[19]. High heating rates reduce the duration of surface diffusion; this condition favors the sinterability of powder systems, and densification is intensified by grain-boundary diffusion while grain growth is hindered[20]. This method has attracted considerable attention as a rapid sintering method that has excellent energy density control. It is also capable of producing highly dense, homogeneous, nanostructured sintered components.[21]

1.2 Nanostructured ferritic alloy

In nuclear reactors, where materials are exposed to very high irradiation doses at high temperatures, several core structures such as fuel cladding are required to maintain mechanical integrity[22, 23, 24]. Given their excellent creep and irradiation resistances, nanostructured ferritic alloys (NFAs) are considered primary candidate materials for both fission and fusion reactors[2]. NFAs are a mixture of mechanically alloyed particle-hardened materials of a nano-grained Fe–Cr alloy matrix and Y–Ti–O–Cr–Fe enriched nanoclusters[1, 25, 26]. NFAs usually present uniform and fine microstructures[25, 26]. Compared with conventional oxide dispersion strengthened (ODS) steels, NFAs possess significantly improved high-temperature strength and radiation resistance[26, 27]. These improvements are believed to be caused by the presence of uniformly dispersed nanoclusters. These nanoclusters prevent dislocation glide, grain growth, and grain boundary slip and also act as sinks for trapping of helium atoms and radiation-generated point defects. In addition, NFAs exhibit excellent creep resistance, high-temperature strength, and highly delayed radiation effects because of the prominent thermal stability of nanoclusters[1, 2, 28, 29, 30, 31]. The elemental composition of the NFA we used is: Fe(Balance)-9Cr-2W-0.4Ti-0.2V-0.12C-0.3Y_2O_3.

1.3 SiC-NFA composite

The nuclear industry places high demands on high-temperature structural alloys[32] and requires materials that are superior to conventional steels and nickel-based super alloys. Over the years, SiC demonstrated technological importance for nuclear application because of its refractory nature (e.g., high melting point and high decomposition temperature) and low neutron absorption[14, 18]. However, the intrinsic brittleness of SiC at all temperature ranges

limits its application. Therefore, the SiC matrix composite, a unique engineered material that is based on the SiC matrix, reinforced metal, and a thin compliant layer between the matrix and metal (interphase), was investigated and developed[33, 34, 35, 36, 37, 38, 39]. Such a composite has a relatively ductile metal phase that is designed to allow plastic deformation, absorb energy, and impede crack propagation in a material that is generally highly brittle[40]. The SiC matrix composite as a structural material can withstand a temperature range that metallic structural materials cannot and can also tolerate a chemically harsh environment where refractory metals (e.g., W and Mo) are often inapplicable because of their strong affinity with interstitial impurities, such as O_2 and N_2 that cause severe embrittlement.

With regard to reinforced metals, NFAs, which are also called ferritic ODS alloys, could be one of the priority options. NFAs are reported to have high strength for various nuclear reactor applications, e.g., the first-wall structure of helium or liquid metal-cooled fusion reactors, because of their excellent creep strength and resistance to high doses of irradiation[41, 42]. Fracture toughness at elevated temperatures could also be significantly improved by appropriate thermo-mechanical treatments[1, 2].

An Ashby map showing yield strength (σ_y) versus Young's modulus (E) ranges at room temperature for foams, natural materials, elastomers, ceramics, polymers, composites, and metals along with the data on SiC and NFAs is presented in Fig. 1.1. The data on NFAs were obtained from literature[1, 2], and the data on other materials were obtained from the database[3]. Both SiC and NFAs have better combination of mechanical properties of strength and modulus than their conventional structural alloy counterparts. Therefore, the combination of these two materials to produce an improved composite is promising.

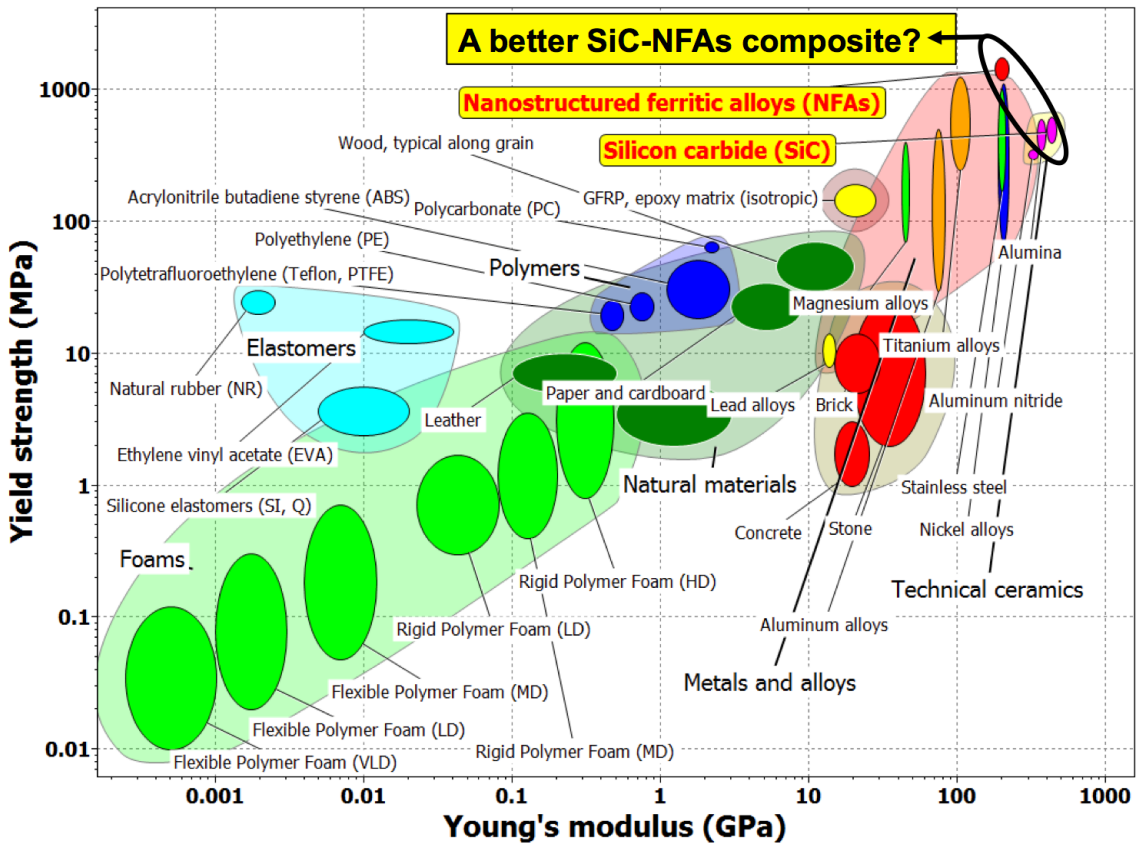

Fig. 1.1 Ashby map showing yield strength (σ_y) versus Young's modulus (E) ranges at room temperature for foams, natural materials, elastomers, ceramics, polymers, composites, and metals along with the data on SiC and NFAs. The data on NFAs were obtained from literature[1, 2], and the data on other materials were obtained from the software[3]. Both SiC and NFAs have better combination of mechanical properties of strength and modulus than their conventional structural alloy counterparts.

1.4 Spark plasma sintering

SPS is a sintering technique that employs uniaxial force and pulsed electrical DC under a vacuum to perform high-rate sintering of powders[43]. SPS has significant advantages in material processing that traditional sintering methods do not have. SPS consists of several applications of high temperature, high applied pressure, and low-mode (low voltage, high current) field (plasma) assisted sintering[44]. Joule heat, which is generated from the electric field, provides the conditions of hot compaction; densification and the final grain structures are also enhanced significantly by the current[45, 46]. The SPS process potentially maintains the microstructure and final grain size in nanosized powder materials after consolidation[45, 46]. Furthermore, it significantly shortens the processing time and improves performance. The application of very high heating and cooling rates is possible because of this direct manner of

heating, and densification is enhanced over grain-growth-promoting diffusion mechanisms. Thus, the intrinsic properties of nanopowders in their fully-dense products are maintained[47, 48].

The samples are placed between the graphite die and punch in the vacuum chamber and held between electrodes. Under pressure and energized pulse, the temperature can quickly increase to 1000 °C–2500 °C, and the heating rate can reach 1000 °C/min[47, 48].

SPS is the sintering of powders under current and pressure. The three factors that contribute to the rapid densification process are mechanical pressure, rapid heating rate, and pulsed DC.

1.4.1 Mechanical pressure

When powders are sintered under applied pressure, the applied pressure results in increased densification at the same temperature[43]. The effect of mechanical pressure can be understood from two roles: mechanical and intrinsic. In the mechanical role, the applied pressure helps in the re-arrangement of particles and destruction of agglomerates. In the intrinsic role, the driving force for sintering also relies on the applied pressure[43].

$$\frac{d\rho}{(1-\rho)dt} = B\left(g\frac{\gamma}{x} + P\right) \tag{1.1}$$

where ρ is the fractional density, B is a term that includes the diffusion coefficient and temperature, g is a geometric constant, γ is the surface energy, x is a parameter that represents particle size, t is time, and P is the applied external pressure. $Bg\frac{\gamma}{x}$ represents the intrinsic driving force for sintering, and BP represents the intrinsic contribution to driving force by the applied pressure. Thus, the significance of the applied pressure depends on the size of particles. When the particle size is small, the term of $Bg\frac{\gamma}{x}$ is large; consequently, the relative contribution of pressure is small. When the particle size is large, the relative contribution of pressure is large[43, 49].

The effect of pressure can also be understood from the perspective of chemical potential. The chemical potential at a particle interface under stress is[43, 50]

$$\mu_{\mathrm{I}} = \mu_{\mathrm{i}}^{0} - \sigma_{\mathrm{n}}\Omega_{\mathrm{I}} \tag{1.2}$$

where μ_{I} is the chemical potential, μ_{i}^{0} is the standard chemical potential, Ω_{I} is the atomic volume of the diffusing species, and σ_{n} is the normal stress at the interface. The tensile stress for σ_{n} is positive, and the compressive stress is negative. Applied pressure provides compressive stress, so the relative contribution of pressure is significant when the particle size is large.

As a result of the applied pressure, the sintering temperature decreases, and grain growth is restricted.

1.4.2 Rapid heating rates

The heating rates of SPS can reach 1000 °C/min[47, 48]. The heat transfer from the die to the compact is highly efficient in this process because the die itself acts as a heating element. Grain size shows a strong dependence on low heating rates, and grain size decreases when the heating rate increases from 50–200 °C/min[48]. Zhou et al.[51] showed that in the range 50–300 °C/min, the heating rate has no marked influence on the final density but has a significant effect on grain size. Specifically, grain size decreases with the increase in heating rate. Rapid heating rates decrease grain growth, so the products sintered by SPS tend to have improved performance because of the small grain size.

1.4.3 Pulsed DC

The major difference between conventional hot pressing and SPS methods is the pulsed DC. In hot pressing, the sample and the die are heated by radiation from an enclosed furnace. However, in SPS, the sample and the graphite die are heated by Joule heat that originates from the current passing thorough them[43]. In addition to providing heat, pulsed DC also creates plasma. This pulse generates spark discharges and even plasma between particles. This is why this sintering process is called “spark plasma sintering.” The plasma exerts a cleansing effect on the surface of the particles, which leads to sintering enhancement. Although many people believe that the current can generate the plasma, experimental evidence on the spark discharge and plasma remains lacking[52, 53]. Several others doubt the existence of the plasma because of the lack of accurate experimental evidence[53, 54].

1.5 Objective

The ultimate objective is to fabricate gradient-structured NFA–SiC composites working as core materials for nuclear reactors. Inside, the pure NFA aims to resist radiation. Outside, the pure SiC aims to strengthen the structure and resist oxidation. Between the two materials, a gradient structure is created, wherein the composition of NFA and SiC gradually changes. Similarly, the properties of the composites gradually change. In this study, a small amount of SiC addition to the NFA matrix and a small amount of NFA addition to the SiC matrix were studied. In addition, carbon coating was utilized to prevent the reaction between NFA and SiC. Gradient-structured NFA–SiC green samples were successfully fabricated.

The objective of this work is to study the addition of NFA to SiC, the addition of SiC to NFA, the reaction between NFA and SiC, and the fabrication of green samples.

2 Study of Spark Plasma Sintered Nanostructured Ferritic Alloy with SiC addition

2.1 Introduction

Cladding materials for nuclear fission and fusion energy systems are exposed to very high doses of neutron irradiation at high temperatures. These materials are required to maintain mechanical integrity over long term operation under such harsh environments [22, 23, 24]. Due to the excellent creep and irradiation resistances, nanostructured ferritic alloy (NFA) materials have been considered as a primary candidate for fission and fusion reactors [2]. The enriched nanoclusters and nanograined Fe-Cr alloy matrix of NFA materials [1, 25, 26] can enable mechanical enhancement and radiation resistance, which traditional oxide dispersion strengthened (ODS) alloys are not able to achieve. The nanoclusters in the NFA alloys not only play the critical role of preventing dislocation glide, grain growth, and grain boundary slip, but also function as sinks to trap helium atoms and radiation-generated point defects. In addition, NFAs have excellent creep resistance, high temperature strength, and highly delayed radiation effects due to the prominent thermal stability of nanoclusters [1, 2, 28, 29, 30, 31]. As a result, NFAs are desirable radiation shielding materials.

Silicon carbide (SiC) [4] is another structural material with high strength and chemical stability, especially in harsh environments. Even when exposed to radiation for a long time, SiC materials [5, 6, 7] still have low induced activation and low after-heat levels. SiC fiber-reinforced SiC-matrix composites (SiC_f/SiC) have prominent structural applications due to the enhanced mechanical properties and damage tolerance [55]. They are being considered as promising candidates for fuel cladding and channel boxes in light water reactors (LWR) and in-vessel components for advanced fission reactors [56, 57, 58].

Composite materials of NFA-SiC are expected to combine these advantages from each component, such as excellent creep and irradiation resistance, corrosion resistance and structure reinforcement. Such a composite would not only take advantage of the plastic deformation and energy absorption from the ductile NFA phase, but also provide the crack-propagation impedance for the highly brittle SiC. Meanwhile, the SiC component in the NFA-SiC composite would enhance high temperature stability and tolerance for chemically harsh environments that pure metallic structural materials cannot withstand. As a result, the addition of SiC should reinforce the NFA matrix while the resistance to radiation is maintained.

In this work, density and microstructure evolution at different sintering temperatures were studied. The effects of the addition of a small amount of SiC on the sintering of the SiC-NFA composites were analyzed. Mechanical properties, such as Vickers hardness, nano-hardness, yield strength, and elastic modulus of the sintered samples, were investigated, and the yield strength was derived from the hardness data.

2.2 Experimental procedures

2.2.1 Sample preparation and sintering

Commercial SiC particles (Grade UF-15, α-SiC, H.C. Starck, Karlsruhe, Germany) and lab-made NFA particles [1, 2] were used as raw materials for pure NFA and NFA-SiC composite sintering. The elemental composition of the NFA is: Fe (Balance)-9Cr-2W-0.4Ti-0.2V-0.12C-0.3Y_2O_3. The NFA particles were screened with a mesh size of No. 653 (20 μm). Mean particle sizes for SiC and NFA were measured using a laser light scattering particle size analyzer (LA-950, HORIBA Scientific, Tenyamachi, Japan). The corresponding sizes were 1.24 μm and 14.28 μm, respectively. Ball milling for the NFA and SiC powders was conducted in order to achieve homogeneous mixing. Then the powders were poured into a cylinder die, which had a diameter of 20 mm. The powder height was controlled at 5 mm. The densification process of the pure NFA and NFA-SiC composites was performed by spark plasma sintering (SPS Nanoceramics, Morton Grove, IL). Main sintering parameters included pressure (100 MPa), heating rate (50^{o}C/min), temperature (850^{o}C, 900^{o}C, 950^{o}C, 1000^{o}C), and holding time (10 min) for the pure NFA, 97.5 vol% NFA-2.5 vol% SiC, and 95 vol% NFA-5 vol% SiC samples.

2.2.2 Characterization

The density of the sintered samples was measured based on the Archimedes method. The phase composition was identified by X-ray diffraction (XRD, PANalytical B. V., Almelo, Netherlands). The microstructure was observed by scanning electron microscopy (FEI FEG-ESEM Quanta600, FEI Company, Hillsboro, OR, USA). Before the SEM observation, the sample surfaces were finely polished and ultrasonically cleaned. The elemental composition was measured by the energy-dispersive X-ray spectroscopy module (EDS, Bruker AXS, MiKroanalysis B. V., Gmbh, Berlin, Germany) attached to the SEM. The average grain sizes were measured from the ethanol-nitric acid etched surface. The statistical estimation for the average grain size was conducted for each sample with the grain number being no less than

150. Vickers hardness was measured by using a macro-hardness tester (LV700AT, LECO, St. Joseph, MI). Fifteen indentations were performed for each sample with a load of 3 kg.

The Vickers hardness was calculated using the following formula [59, 60]:

$$H_V = k\left(\frac{\mathrm{P}}{d^2}\right) \tag{2.1}$$

where k is the shape factor of the indenter, P is the load to the indenter, d is the diagonal length of the indention.

The yield strength was calculated using the following formula [61, 62, 63]:

$$\sigma_{\mathrm{YS}} = \frac{1}{3}\mathrm{H_v} \tag{2.2}$$

where σ_{YS} is the yield strength, which has the unit of GPa.

The nano-hardness was measured by nano-indentation (TI 950 Triboindenter, Hysitron, Inc., Minneapolis, MN). A 100 nm 3-sided pyramidal diamond Berkovich tip was used during the measurement. A nano-indentation array of 15 indents was performed for each sample. The peak load was kept at 4000 μN for all the nano-indents. All the above measurements were conducted at the room temperature.

2.3 Results and discussion

2.3.1 Phase analysis

Fig. 2.1 shows the XRD patterns of the pure NFA, 97.5 vol% NFA-2.5 vol% SiC, and 95 vol% NFA-5 vol% SiC samples at different sintering conditions. All the samples show the well-crystallized α-Fe XRD patterns, and no SiC peaks can be observed. There are new peaks from γ-Fe at 950°C and 1000°C, while there are only peaks from α-Fe at 850°C and 900°C. This is because the onset temperature of the α→γ Fe phase transformation is 948°C [64]. In addition, the 100 vol% NFA sample after 1000°C sintering gives the most obvious peaks from γ-Fe, while the 95 vol% NFA-5 vol% SiC and 97.5 vol% NFA-2.5 vol% SiC samples have only very small peaks from γ-Fe. This means that the addition of SiC delays the Fe $\alpha \rightarrow \gamma$ phase transformation and increases the phase transformation temperature.

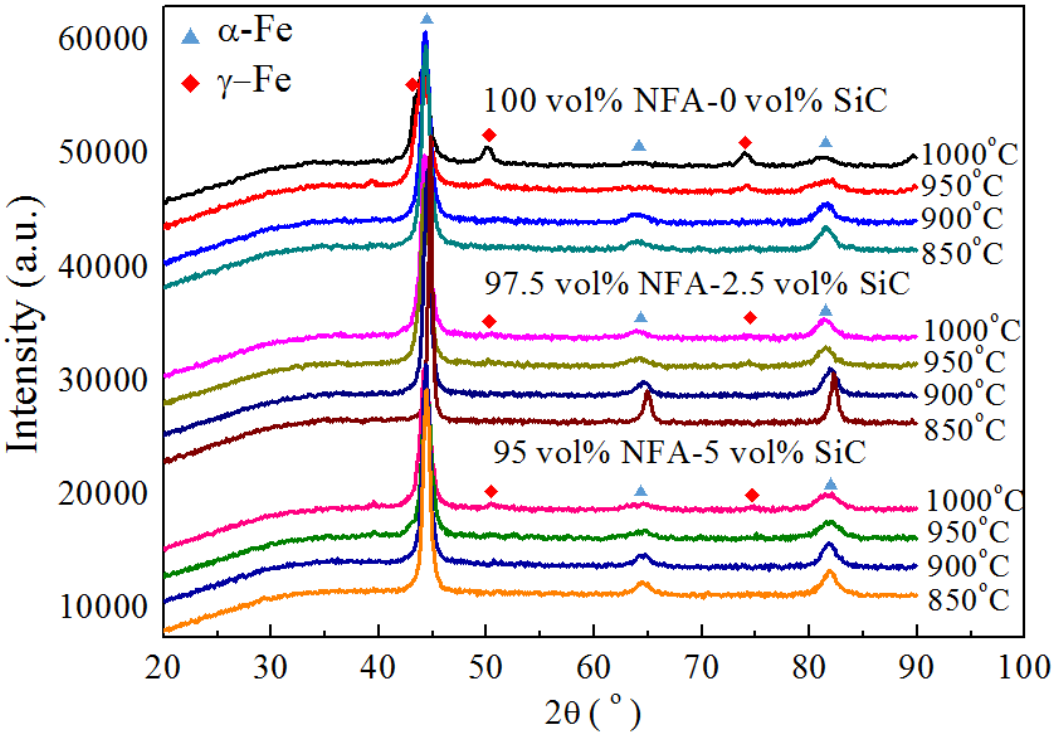

Fig. 2.1 XRD patterns of sintered pure NFA and NFA-SiC composite samples with different temperatures.

Based on the Si-Fe phase diagram [65], when the atomic percent of Si is less than 3.8 at%, the phase transformation temperature increases with the increasing content of Si. In our system, the 95 vol% NFA-5 vol% SiC sample has 3.3 at% of Si. As a result, the phase transformation temperature increases from the 2.5 vol% SiC addition sample to the 5 vol% SiC addition sample. The fundamental process can be understood as follows. When sintering NFA-SiC composites, decomposition occurs and leads to the formation of silicon and carbon at high temperatures [38, 39, 66]. It has been shown that the decomposition of SiC starts at 610°C, then silicon diffuses into the lattice of iron to alloy with iron. The diffusion of silicon tends to destabilize γ-Fe and hinder the phase transformation of α-Fe → γ-Fe, raising the phase transformation temperature [67]. When the atomic percentage of Si is above 3.8, there is no phase transformation from α-Fe to γ-Fe. Thus, the composites with the added SiC tend to have a much smaller content of γ-Fe. This explains why γ-Fe phase could hardly be observed in the 95 vol% NFA-5 vol% SiC composite sample even with sintering at 1000°C.

2.3.2 Microstructure

Fig. 2.2 shows the SEM images of the sintered pure NFA and NFA-SiC composite samples. In Figs. 2.2 (a–d), the microstructures of the pure NFA samples show that the sintered bodies are fairly dense without obvious pores. The NFA-SiC samples in Figs. 2.2 (e–h) and Figs. 2.2 (i–l), however, show different levels of porosity. The 97.5 vol% NFA-2.5 vol% SiC samples and 95 vol% NFA-5 vol% SiC samples have similar change tendencies in pore shape and porosity with the sintering temperature. For both of them, pores tend to become closed and roundish and the pore amount gradually decreases with the increase of the sintering temperature. The major difference is that the latter samples have more pores at the same sintering temperature. It is believed that these pores are mainly from the reaction of NFA and SiC, which will be further discussed in Section 2.3.3, 2.3.4. The bright phases from all the images shown in Fig. 2.3 are believed to be the dispersed oxide nanoclusters from the NFA. The gray phase shown in Fig. 2.2d is probably γ-Fe precipitated from α-Fe at 1000^{o}C, while the gray phase shown near pores in Figs. 2.2 (g–h) is considered to be the products of the reaction between NFA and SiC.

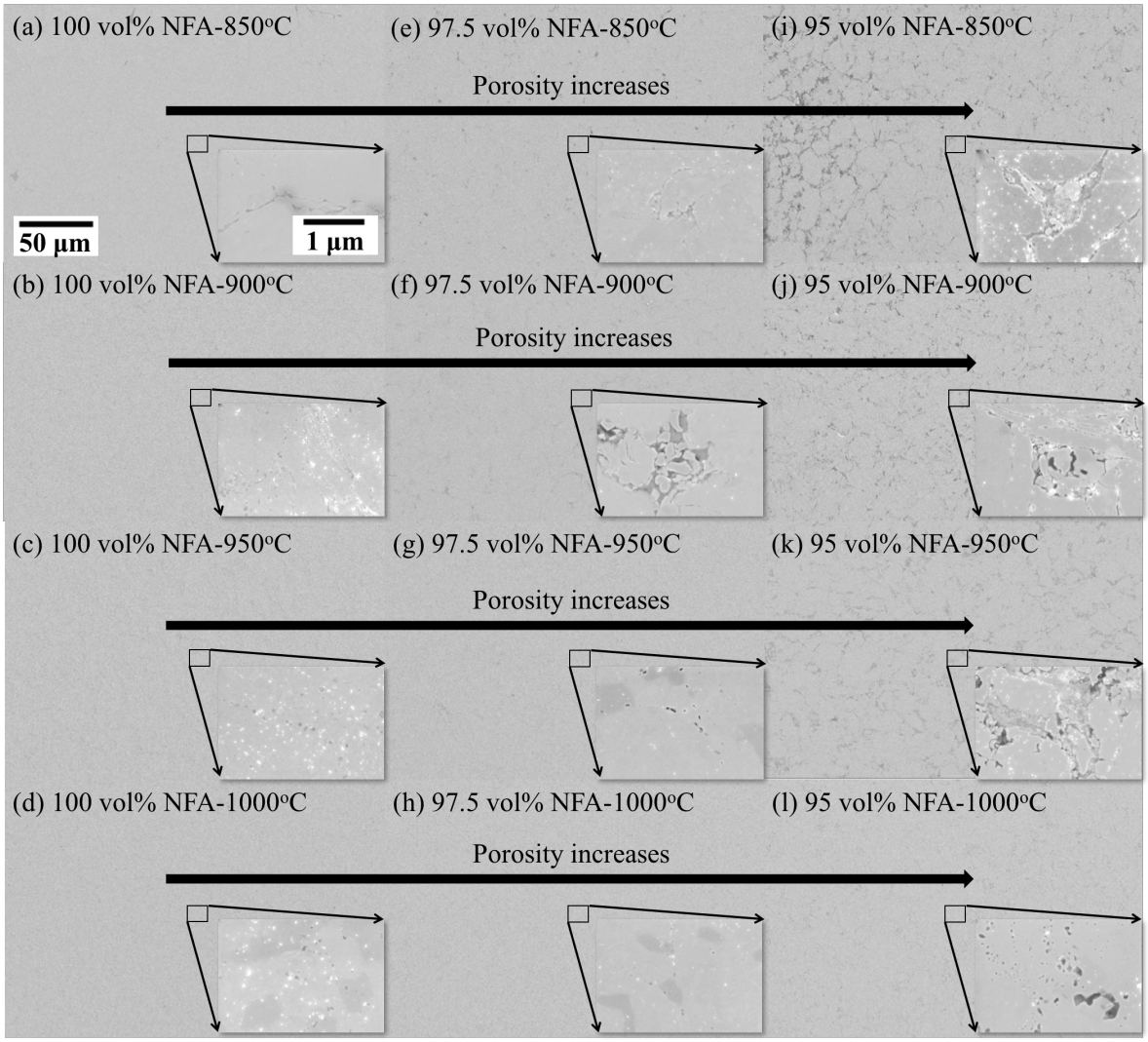

Fig. 2.2 SEM images of pure NFA and NFA-SiC composite samples with different sintering temperatures.

Fig. 2.3 shows the average grain sizes for the pure NFA and the NFA-SiC composites with the sintering temperature at 850°C–1000°C. The representative images from the etched NFA sample sintered at 850°C is shown in Fig. 2.4. The grains and grain boundaries can be observed in Fig. 2.4a. Fig. 2.4b indicates that there are no sub-grains involved in the measured grains. It should be noted that the average grain sizes for all the samples are between 6 µm–8 µm, although the samples are sintered at different temperatures and with different SiC additions. This means that sintering temperatures and SiC additives do not affect the grain size of the NFA phase to a large extent.

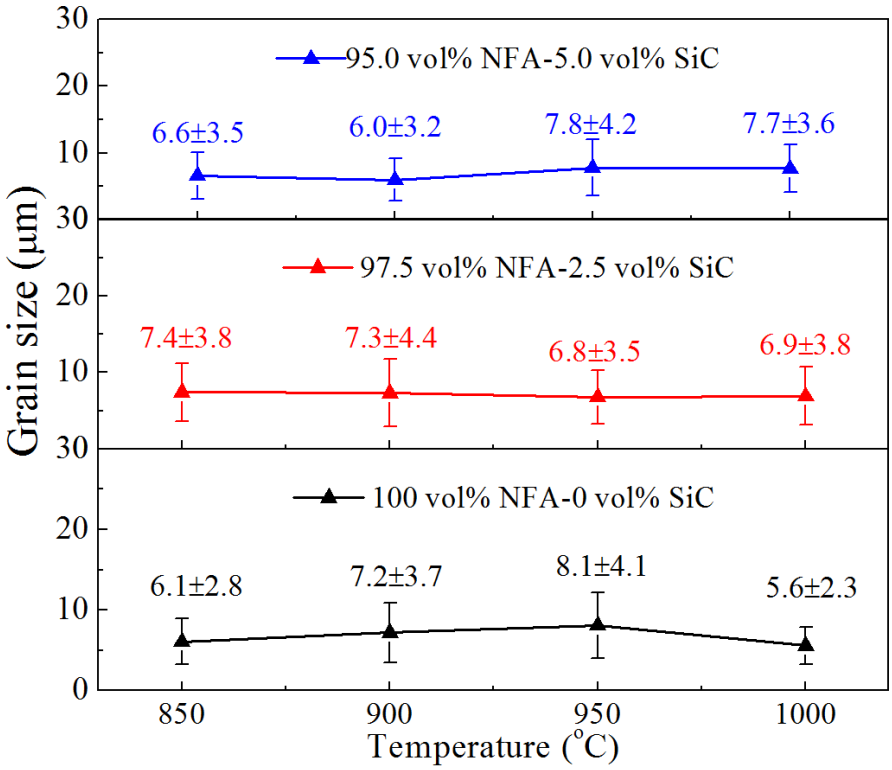

Fig. 2.3 Average grain sizes for pure NFA and NFA-SiC samples with different sintering temperatures.

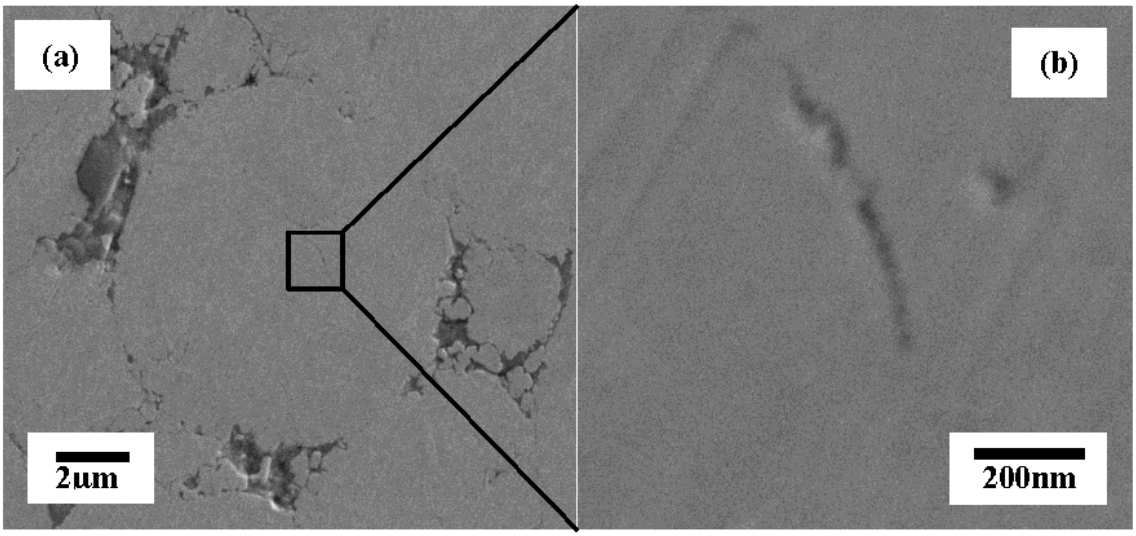

Fig. 2.4 Representative images of the etched NFA sample sintered at 850°C.

2.3.3 Density

Fig. 2.5 shows the relative densities of the pure NFA and NFA-SiC composite samples at different sintering temperatures. The 95 vol% NFA-5 vol% SiC samples have much lower densities than the pure NFA and 97.5 vol% NFA-2.5 vol% SiC samples. The 95 vol% NFA-5 vol% SiC samples have the relative densities of 82±1%, 82±2%, 87±2%, 93±3% from 850°C to 1000°C, while the 97.5 vol% NFA-2.5 vol% SiC samples have the relative densities of 87±1%, 92±1%, 99±1%, 99±2% from 850°C to 1000°C, which are close to those of the pure NFA samples, 96±1%, 95±1%, 98±1%, 101±1%, from 850°C to 1000°C. All the samples show an increasing tendency for the relative densities with the sintering temperature, which indicates enhanced densification with the temperature. The pure NFA samples have the highest relative densities among the three sintered samples at the same sintering temperature. The increase of the SiC content in the NFA matrix tends to cause less densification of the sintered NFA-SiC composites at the same temperature. Such density changes are consistent with the SEM observations of the porosity for all the samples shown in Fig. 2.2 Meanwhile, the NFA-SiC composites with 2.5 vol% SiC nearly reach the high densities close to those of the pure NFA samples at the sintering temperatures of 950°C–1000°C. However, the relative densities of the NFA-SiC composite with 5 vol% SiC are much lower at the same sintering temperature. This is because the reactions between NFA and SiC become more extensive when more SiC is added. The delay of the densification process for the NFA-SiC composites is reflected from the increasing number of pores indicated by the direction of the arrow in Fig. 2.2.

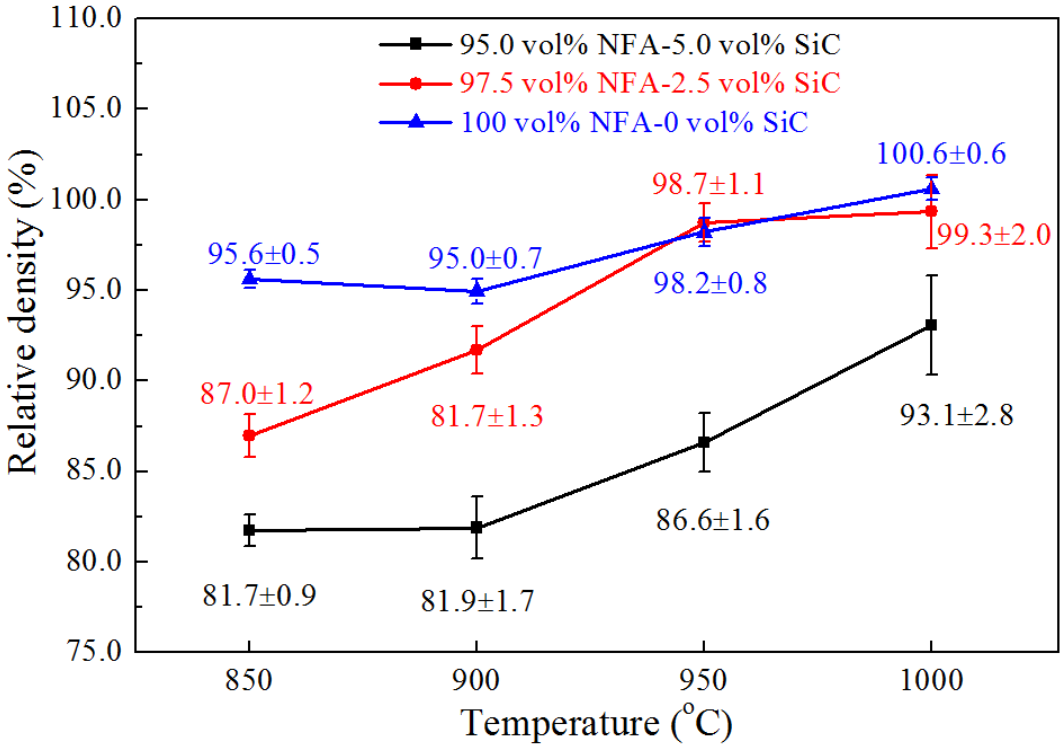

Fig. 2.5 Relative densities of the NFA and NFA-SiC composite samples at different sintering temperatures.

2.3.4 Mechanical properties

Fig. 2.6 shows the Vickers hardness of the sintered pure NFA and NFA-SiC composite samples at different sintering temperatures. The hardness of 6–8 GPa for the sintered pure NFA samples is much higher than the reported values of 3–5 GPa [68] and 2.1 GPa [69]. This is attributed to the small average grain size of 6–8 μm. In Fig. 2.6, the hardness for the NFA-SiC samples is lower than that of the pure NFA samples at 850°C and 900°C. With the increase in the sintering temperature to 950°C and 1000°C, the hardness of the NFA-SiC composites exceeds that of the pure NFA samples. Due to the high ductility of the NFA material, the grain boundaries do not play a critical role for the indentation resistance. Thus, there is no relation with the feature of the average grain size shown in Fig. 2.3 However, the hardness trend shows close correlation with the relative density in Fig. 2.5 Both the relative density and the hardness increase with the sintering temperature. The lower density samples tend to produce lower hardness.

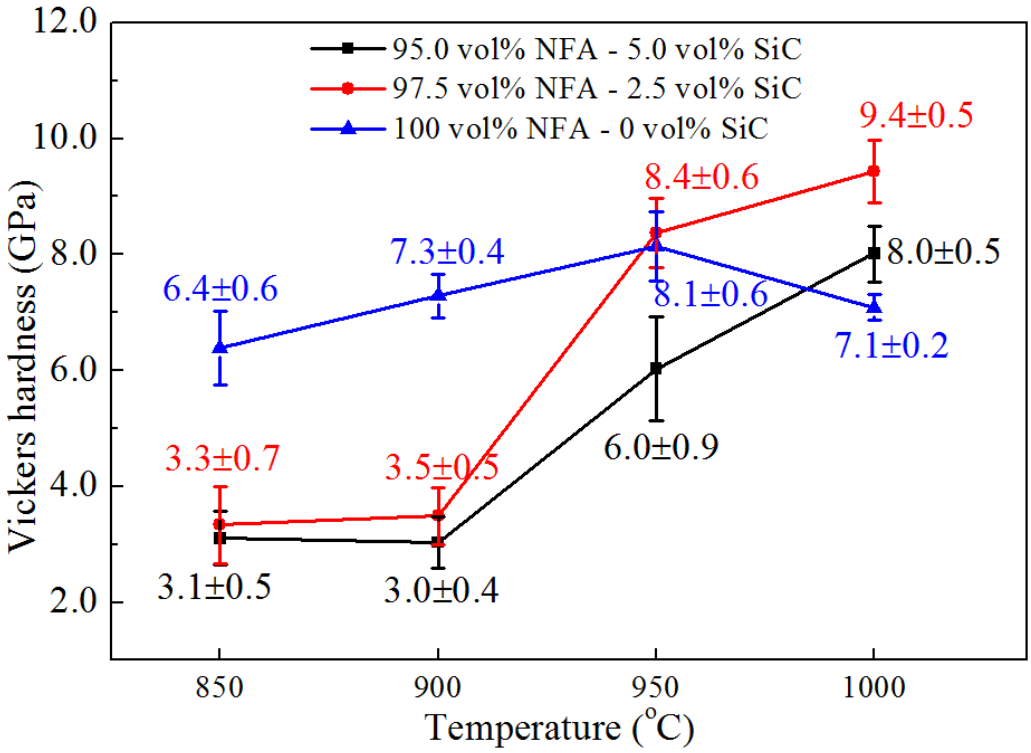

Fig. 2.6 Vickers hardness of the pure NFA and NFA-SiC composite samples at different sintering temperatures.

Another phenomenon is that higher addition of SiC produces lower hardness for the NFA-SiC composites at the same sintering temperature. Thus, the effect of SiC addition on the Vickers hardness is a little complicated for the NFA-SiC composite. This is because during the sintering of the NFA-SiC composites, reactions between NFA and SiC occur as follows: [38, 39, 66]

$$SiC \rightarrow Si + C \quad (2.3)$$

$$Fe + Si \rightarrow FeSi \quad (2.4)$$

$$Fe + 2Si \rightarrow FeSi_2 \quad (2.5)$$

$$3Fe + SiC \rightarrow Fe_3Si + 3C \quad (2.6)$$

$$3Fe + C \rightarrow Fe_3C \quad (2.7)$$

The Gibbs free energy of these reactions is shown in the table below[70, 71]. The unit of Gibbs free energy is kJ/mol. From the Gibbs free energy values shown in the table, iron silicides are the most likely to be produced during the sintering process. The Gibbs free energy of equation (6) shows that the NFA makes the decomposition of SiC easier to happen.

Table 2.1 The Gibbs free energy of different reactions at 850°C, 900°C, 950°C, and 1000°C.

Temperature/°C	SiC=>Si+C	Fe+Si=>FeSi	Fe+2Si=>$FeSi_2$	3Fe+SiC=>Fe_3Si+3C	3Fe+C=>Fe_3C
850	62.52	-73.54	-70.74	-47.45	5.93
900	62.12	-73.53	-70.27	-48.58	5.07
950	61.72	-73.53	-69.81	-49.70	4.22
1000	61.31	-73.53	-69.34	-50.83	3.37

Even though based on the Si-Fe phase diagram [65], there should be no iron silicide formation due to the low Si content in our system (Si<3.8 at%), the reaction still occurs. The reason is that Si is not distributed homogeneously in the composites. It has a much higher content at the interface between NFA and SiC. After sintering, newly formed phases of iron silicides or iron carbides (Fe_3Si, FeSi, $FeSi_2$, and Fe_3C) in the NFA-SiC composite change the microstructures. SiC decomposition and newly formed products lead to a porous structure, which can be seen from the images in Figs. 2.2 (e–h) and (i–l). When more SiC is added, the reactions between NFA and SiC become more intensive, thus producing lower amounts of hardness.

When the sintering temperature increases to 950°C, the hardness of the 5 vol% SiC samples is much lower than that of 2.5 vol% SiC addition samples, even slightly lower than that of the pure NFA samples. This is also due to the porous microstructure come from the reactions between SiC and Fe. However, the effect of the reactions has been balanced by the effects of SiC/products and the increased sintering temperature, which are also reflected in Figs. 2.2 (e–h) and (j–l). For example, the 97.5 vol% NFA and 95 vol% NFA samples have higher density and lower porosity after 1000°C sintering than those sintered at 850°C. Meanwhile, the 97.5 vol% NFA sample at 950°C sintering temperature has almost the same relative density (99±1%) as that of the pure NFA sample (98±1%), and these two samples also show almost the same hardness value. This is because the positive effect of the SiC addition is balanced by the negative effect of the reactions.

It should be noted that there is an initial increase (up to 950°C) and then a subsequent deterioration (at 1000°C) in hardness for the pure NFA samples after sintering. The hardness of the sample sintered at 1000°C has a lower hardness value of 7.1±0.2 GPa. This is believed to be caused by the precipitation of the secondary γ-Fe phase from the α-Fe matrix phase. As shown in Fig. 2.1, there is a relatively high content of γ-Fe after sintering at 1000°C. Therefore, the decrease of the hardness is related to the $\alpha \rightarrow \gamma$ iron phase transformation, because γ-Fe has a lower hardness than α-Fe (3.75±0.23 GPa for α-Fe, 3.19±0.16 GPa for γ-

Fe [72]). In addition, due to the short sintering time, the newly formed γ-Fe phase cannot be fully densified, which subsequently weakens the microstructure and further decreases the hardness of the pure NFA sample.

To understand the effect of nano-scale local structure on the hardness, an array of nano-indents has been created continuously by automation indentation. Because the size of the nano-indenter tip is only 100 nm, the measurement is very location-specific and the measured values can avoid the effect of pores. The nano-hardness of the 100 vol% NFA, 97.5 vol% NFA-2.5 vol% SiC, and 95 vol% NFA-5 vol% SiC samples after 1000^{o}C sintering is 8.0±1.7 GPa, 15.9±0.9 GPa, and 14.9±0.7 GPa, respectively. This confirms the changing trend of the Vickers hardness for the samples sintered at 1000^{o}C. Addition of SiC improves the nano-hardness of the NFA-SiC composites.

The effect of the reaction products on the nano-hardness has also been studied. Nano-hardness values and the corresponding local chemical compositions of different indents for the 97.5 vol% NFA-2.5 vol% SiC sample at 900^{o}C sintering temperature are presented in Table 2.2. The indent Nos. 1, 3, and 4 have lower hardness values, while the indent Nos. 2, 5, and 6 show higher nano-hardness values. The regions with higher nano-hardness values contain more Fe, and less C and Si. For example, No. 3 has the nano-hardness of 8.3 GPa with 82.0 wt% Fe, 5.6 wt% C, and 2.0 wt% Si. The regions with lower nano-hardness values contain less Fe, and more C and Si. For example, No. 2 has the nano-hardness of 12.1 GPa with 87.0 wt% Fe, 3.1 wt% C, and 0.4 wt% Si. This means that SiC dispersed in those regions and reacted with NFA, the reaction products led to lower nano-hardness for the NFA-SiC composites.

Table 2.2 Nano-hardness and the corresponding elemental compositions at local regions for the 97.5 vol% NFA-2.5 vol% SiC sample sintered at 900^{o}C (the size of each area for EDS measurement is about 3.5 μm×2.7 μm).

Indentation No	**Hardness/GPa**	**Fe/ wt%**	**Cr/ wt%**	**C/ wt%**	**Si/ wt%**
1	7.7	83.5	8.6	6.4	1.5
2	12.1	87.0	9.5	3.1	0.4
3	8.3	82.0	10.4	5.6	2.0
4	7.5	83.5	10.1	4.9	1.5
5	11.4	86.8	9.7	3.0	0.5
6	11.8	86.1	9.5	3.2	1.2

The yield strength is obtained as shown in Fig. 2.7. Because the yield strength is obtained from the Vickers hardness, they show the same trend. In the literature, the yield strength is reported to be 1.45 GPa for 14YWT NFA steel [73], 0.96 GPa for ODS-EUROFER steel [73], and 1.20 GPa for 12Cr-ODS steel [74]. Our pure NFA samples have a much higher yield strength of 2.13–2.72 GPa than the reported values. Obviously, the SPS method can enhance the mechanical property of the NFA steel. Although the NFA-SiC composites sintered at 850°C–900°C show relatively lower yield strength of 1.03–1.16 GPa, they have higher yield strength of 2.01–3.14 GPa when the sintering temperature is increased to 950°C–1000°C. Especially, for the 97.5 vol% NFA-5.0 vol% SiC sample, the yield strength is 2.0 ± 0.3 GPa at 950°C and 3.14 ± 0.18 GPa at the sintering temperature of 1000°C, which are much higher than that of the pure NFA samples at the same sintering temperature. This means that the NFA-SiC composite could be a promising high strength composite material for nuclear applications.

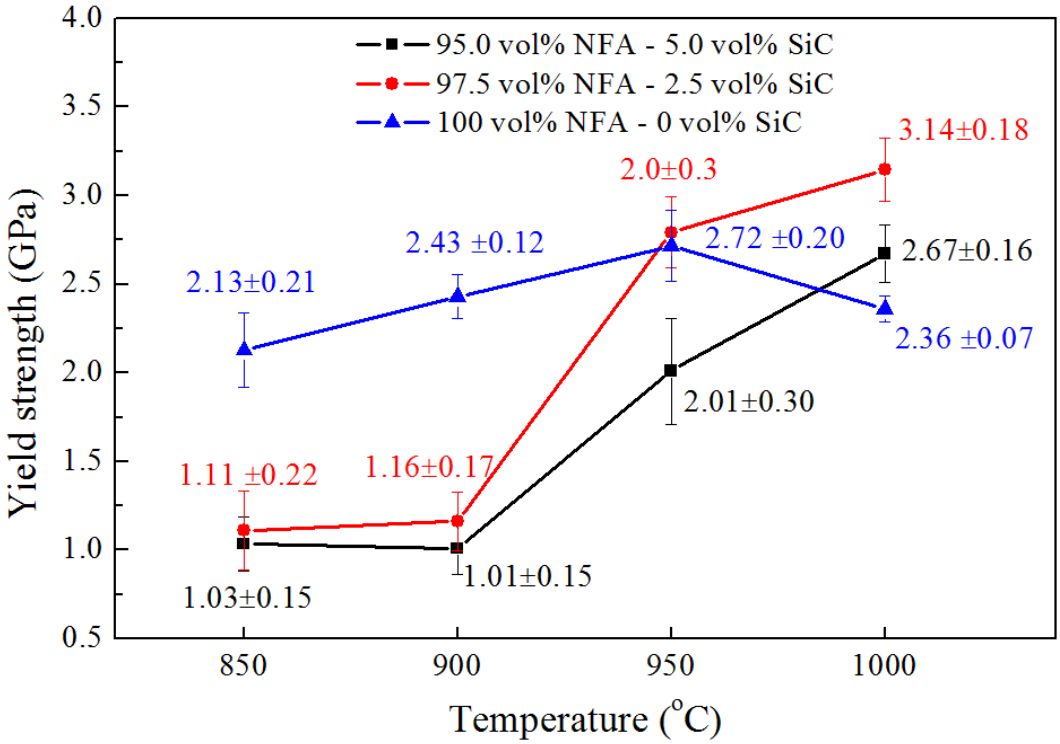

Fig. 2.7 Yield strength of the pure NFA and NFA-SiC samples at different sintering temperatures.

The elastic modulus values are obtained along with the nano-hardness during the nano-indentation test and presented in Fig. 2.8. The 100 vol% NFA sample has the highest elastic modulus, and the 95 vol% NFA-5 vol% SiC sample has the lowest elastic modulus. The addition of SiC decreases the elastic modulus of the composites. This is because the

reaction products between NFA and SiC have a lower elastic modulus than the pure NFA. Thus, the composite containing more SiC has a lower elastic modulus.

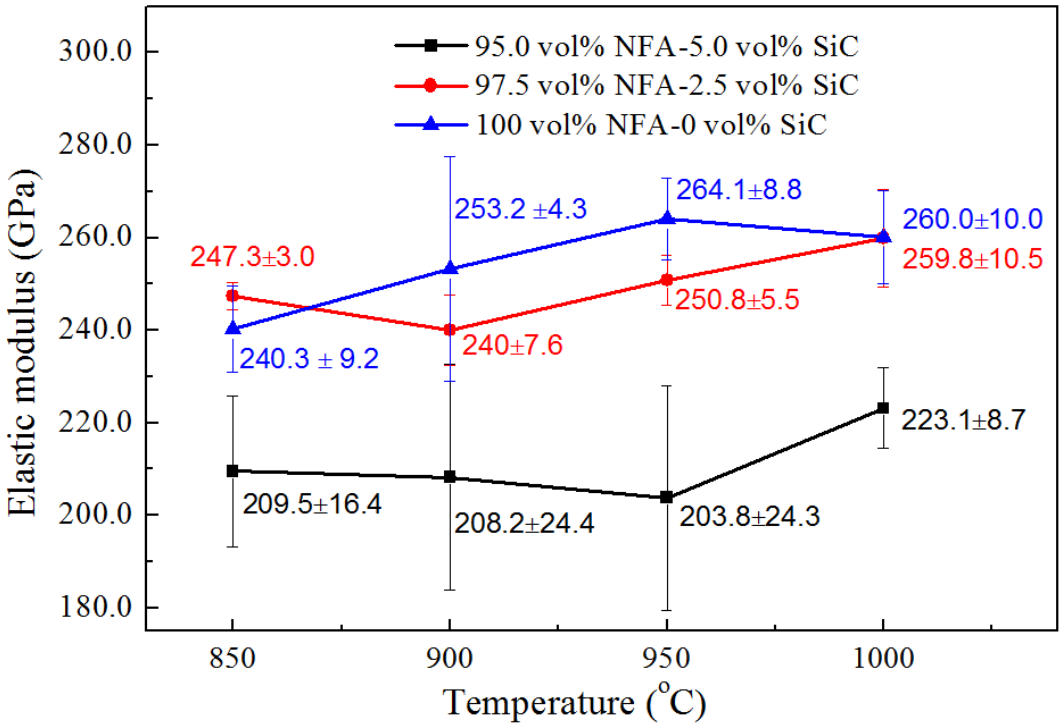

Fig. 2.8 Elastic modulus of the pure NFA and NFA-SiC samples with different sintering temperatures.

2.4 Conclusions

In this work, pure NFA samples and SiC-NFA composite samples were prepared using SPS sintering method. Their phase composition, microstructure, density, Vickers hardness, yield tensile strength, nano-hardness, and elastic modulus were investigated. Both the pure NFA and NFA-SiC samples show the main phase of α-Fe but some γ-Fe phase is present between 950°C and 1000°C. SiC addition delays γ-Fe formation from α-Fe, but also leads to more porosity. The average grain sizes are 6–8 μm for all the samples. The densification process is inhibited by the increase of SiC content. The NFA-SiC composites have lower Vickers hardness than the pure NFA at the lower sintering temperature of 800°C and 900°C, but higher Vickers hardness at higher sintering temperature of 1000°C. Meanwhile, higher content of SiC adversely lowers the Vickers hardness of the NFA-SiC composites. The diffusion and reaction between NFA and SiC lead to lower overall hardness for the NFA-SiC composites. The estimated yield strength of the NFA-SiC composite is

higher than that of the pure NFA at the higher sintering temperature of 950^{o}C–1000^{o}C. The pure NFA sample has higher elastic modulus, and the reaction between NFA and SiC decreases the elastic modulus of the NFA-SiC composites.

3 Study of Spark Plasma Sintered Silicon Carbide with Nanostructured Ferritic Alloy Addition

3.1 Introduction

Silicon carbide (SiC) is a well-recognized engineering material [4] for mechanical strength as well as for physical and chemical stability up to very high temperatures. The exceptional stability under high radiation exposure[5, 6, 7] makes it an alternative material in harsh radiation environments, such as fission and fusion nuclear reactors, due to the low induced activation and low after-heat properties. At high temperatures, the impurities in SiC show extremely low diffusivities, which makes it quite different from traditional nuclear materials. Thus, SiC is being used as fission product barriers in the TRISO fuel [8]. SiC coating layer for fission fuel particles is effective for the retention of solid fission products at temperatures exceeding 2000 K [9, 10]. As a result, SiC-based ceramic composites are expected to be promising structural materials in fission energy systems.

From the processing point of view, SiC is a highly covalently-bonded compound. [11] It is difficult to densify SiC without sintering additives based on the conventional methods. Although sintering additives [12, 13], including boron-based compounds, yttrium oxide, and aluminum oxide, are used to promote SiC densification and its mechanical properties [15, 16] by introducing a liquid phase at grain boundaries, these additives are detrimental to the irradiation performance, such as neutron absorption, cause swelling [14], and limit the nuclear applications. In order to achieve full density for SiC but avoid these drawbacks, sintering SiC with nanoparticles without any additives [13, 14] is reported to achieve high density and improve the mechanical properties by using spark plasma sintering (SPS). Densification of SiC ceramics with additives [12, 17] is also demonstrated by using SPS.

Nanostructured ferritic alloys (NFAs) are defined as a mixture of mechanically-alloyed and particle-hardened material with nano-grained Fe-Cr alloy matrix and Y-Ti-O-Cr-Fe enriched nanoclusters [1, 25, 26]. Due to the excellent creep and irradiation resistances, NFAs have been considered as the primary candidate materials for both fission and fusion reactors [2]. A small amount of NFA addition to SiC can potentially enhance the creep and irradiation resistances of SiC. Furthermore, due to the low melting point of NFA, the sintering of SiC can be accelerated, which would make it easier for SiC to achieve full density.

In this work, pure SiC and NFA-SiC composites (2.5 vol% NFA-97.5 vol% SiC and 5.0 vol% NFA-95.0 vol% SiC) were sintered between 1950^{o}C and 2100^{o}C by SPS. The density, phase, and microstructure were studied. Mechanical properties including Vickers hardness, flexural strength, and nano-hardness were characterized.

3.2 Experimental procedures

Commercially available SiC particles (SiC UF-15, H. C. Starck, Goslar, Germany) and lab-made NFA particles [1, 2] were used as raw materials. The mean particle sizes for the SiC and NFA were measured by a laser light scattering particle size analyzer (LA-950, HORIBA Scientific, Tenyamachi, Japan). The corresponding mean sizes were 1.24 μm and 14.28 μm, respectively. The volume ratios for the NFA and SiC in the two NFA-SiC composites were 97.5:2.5 and 95.0:5.0, respectively. Ball milling of the SiC and NFA powders was initially carried out for 60 min before the sintering process. Subsequently, the powders were poured into a cylinder die for the SPS process, which had 20 mm diameter and the height of the powders was controlled at about 5 mm. Sintering for both the pure SiC and the NFA-SiC composites was performed at 100 MPa pressure, a100^{o}C/min heating rate, and a 10 min holding time. The peak temperatures were 1950°C, 2000°C, 2050°C, and 2100^{o}C, respectively.

The density of the sintered samples was measured by a gas pycnometer (AccuPyc II 1340, Micromeritics, Norcross, GA). The phase composition was measured by X-ray powder diffraction (XRD, PANalytical B.V., EA Almelo, Netherlands). The microstructure was characterized by electron scanning microscopy (SEM, Quanta 600 FEG; FEI Company, Hillsboro, OR). The elemental composition was measured by an energy dispersive X-ray spectroscopy module (EDS, Bruker AXS, MiKroanalysis, Gmbh, Berlin, Germany), which was attached to the SEM. The Vickers hardness was obtained from 15 indentations with a load of 10 kg by using a hardness tester (LV700AT, LECO, St. Joseph, MI). The nano-indentation was implemented by using a nano-indenter (TI 950 Triboindenter, Hysitron, Inc., Minneapolis, MN) with a 3-sided pyramidal diamond Berkovich probe of 100 nm. The load was kept at 8000 μN.

3.3 Results and discussion

3.3.1 Density

Fig. 3.1 shows the relative density of the sintered pure SiC and NFA-SiC samples at different sintering temperatures. The 2.5 vol% NFA-97.5 vol% SiC samples have the highest relative densities (near 100%) at the sintering temperatures of 1950°C and 2000°C. The 5.0 vol% NFA-95.0 vol% SiC samples have the lowest relative densities (91–94%) at the same sintering temperatures. The pure SiC samples have the relative densities (94–99%) in between the two composite samples in the sintering temperature range of 1950°C–2000°C. This means that the addition of 2.5 vol% benefits the densification of the NFA-SiC composites, while higher NFA content of 5.0 vol% NFA hinders the densification of the NFA-SiC composites. As an example, the 2.5 vol% NFA-97.5 vol% SiC sample has the highest relative density of ~100% at 2000°C, while the 5.0 vol% NFA-95.0 vol% SiC sample has the lowest relative density of ~92% at the same temperature. These results can be understood as follows.

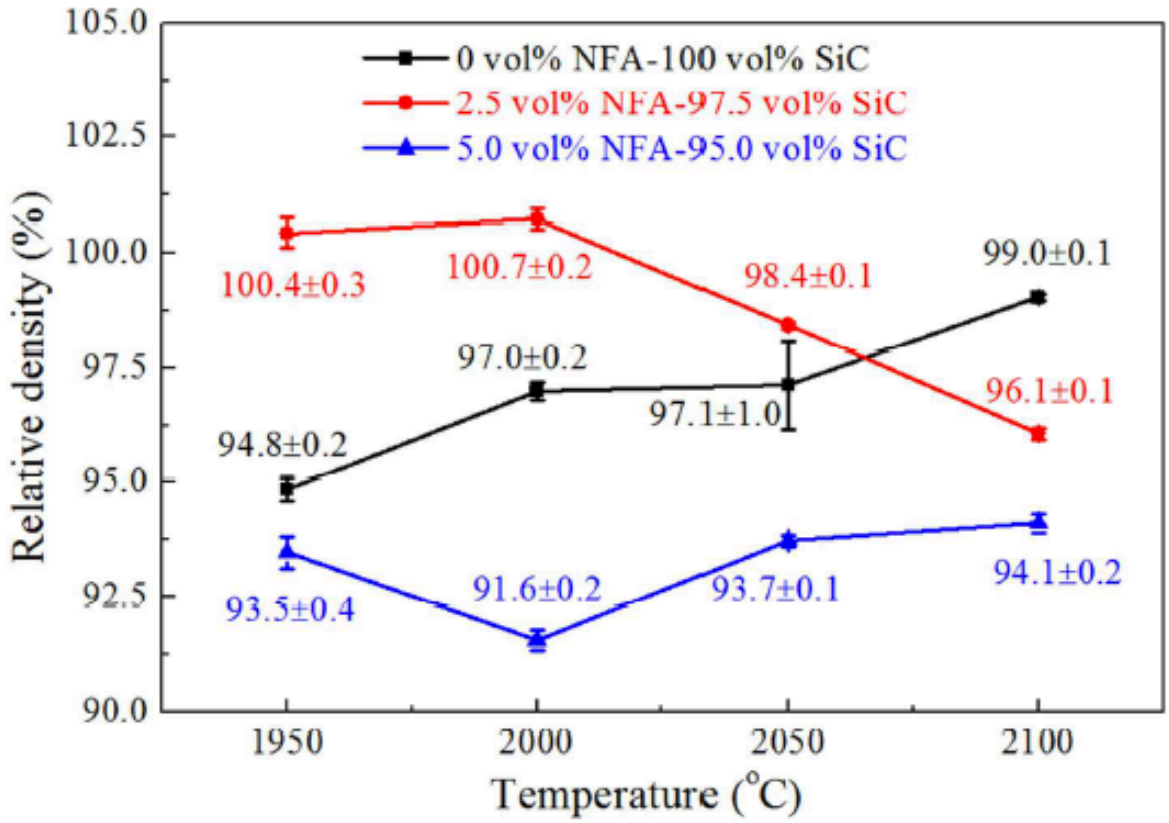

Fig. 3.1 Relative density of the pure SiC and NFA-SiC samples at different sintering temperatures.

The melting point of NFA is about 1500°C, while the melting point of SiC is about 2700°C. The sintering of the NFA-SiC composites at the temperatures between 1950°C and 2100°C can be considered as liquid phase sintering. The liquid melts of NFA move into the inter-particle areas of the SiC and facilitate the densification of the NFA-SiC composites. It is reported that α-SiC ceramics [75] can achieve full density by hot pressing, with the addition of Y_2O_3-Al_2O_3 as the liquid phase. However, the reactions between NFA and SiC at these high sintering temperatures cause the decomposition of SiC, and introduce new silicides ($FeSi_2$) and carbon-rich phases (Fe_3C and C). This subsequently impacts the densification of the composites. (Figs. 3.3 and 3.4 show the carbon-rich phase from the decomposition of SiC; Fig. 3.6b and Table 3.1 show the possible reaction products—the silicides phases). As a result, a small amount of NFA (e.g., 2.5 vol%) benefits the densification of the composites due to the liquid phase formation. However, a high amount of NFA (e.g., 5.0 vol%) compromises the densification of the composites because of the negative effect of the reactions between NFA and SiC.

As expected, the relative density of the pure SiC sample increases with the sintering temperature. Without any detrimental reactions between SiC and NFA, the pure SiC samples have much higher relative densities than the 5.0 vol% SiC-95.0 vol% NFA samples. However, the relative density of the 2.5 vol% NFA-97.5 vol% SiC sample declines when the sintering temperature is higher than 2000°C. This indicates that the 2.5 vol% NFA-97.5 vol% SiC samples should be sintered at lower temperatures of 1950°C–2000°C to achieve full density. More silicide products and carbon-rich phases are produced with the increase in sintering temperature, which decreases the relative density of the 2.5 vol% NFA-97.5 vol% SiC samples. The relative density of the 5.0 vol% NFA-95.0 vol% SiC sample does not change significantly at different sintering temperatures, probably because the positive effect of the liquid phase sintering is balanced by the negative effect of the reaction products of silicide phases and carbon-rich phases in the entire temperature range.

3.3.2 Phase

Fig. 3.2 shows the XRD patterns of the pure SiC and NFA-SiC samples at different sintering temperatures. The pure SiC and NFA-SiC samples have the same XRD patterns after sintering between 1950°C and 2100°C. At 45°C, there is a small peak from $FeSi_2$. All the XRD peaks are from the α-SiC phase. The highest peak has the miller index (006) located at 35.7°C, while the other four main peaks are indexed as (101) at 34.1°C, (103) at 38.2°C, (108) at 60.0°C, and (116) at 71.8°C.

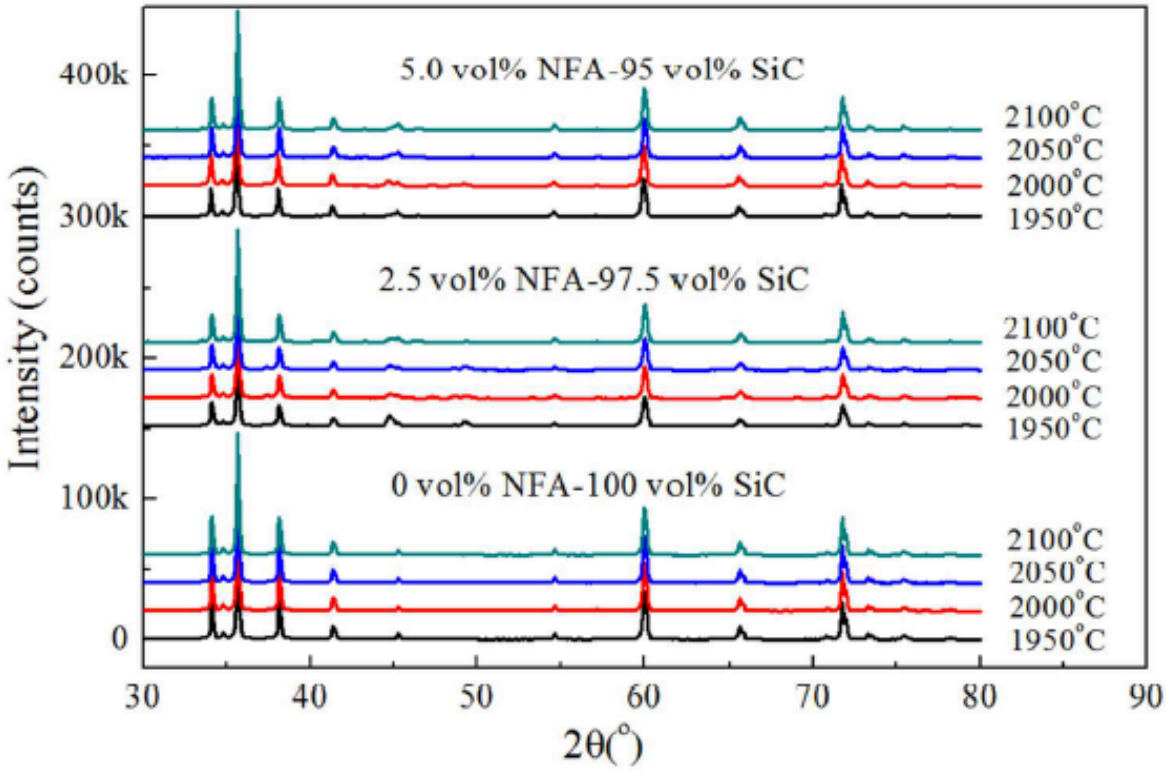

Fig. 3.2 XRD patterns of the pure SiC and NFA-SiC composite samples at different sintering temperatures.

3.3.3 Microstructure

Fig. 3.3 shows the SEM images of the fracture surfaces of the pure SiC and NFA-SiC composite samples at different sintering temperatures. These samples exhibit differences in morphology due to the different compositions. The pure SiC samples have a relatively smooth fracture surface, while the two NFA-SiC composites have a rougher fracture surface. Thus, the addition of NFA to the SiC matrix modifies the microstructure of the sintered NFA-SiC composite samples. The pure SiC samples have the densest fracture surface throughout the sintering range of 1900°C–2100°C, and it is difficult to observe any pores on the fracture surfaces. Even at the lowest sintering temperature of 1950°C, the pure SiC sample (with some small pores) is still denser than that of the NFA-SiC composite samples as shown in Figs. 3.3a, 3.3e, and 3.3i. When the sintering temperature increases to 2100°C, it is difficult to see any pores on the pure SiC fracture surface. This further explains why the pure SiC samples have increasing densities with the sintering temperature as shown in Fig. 3.1.

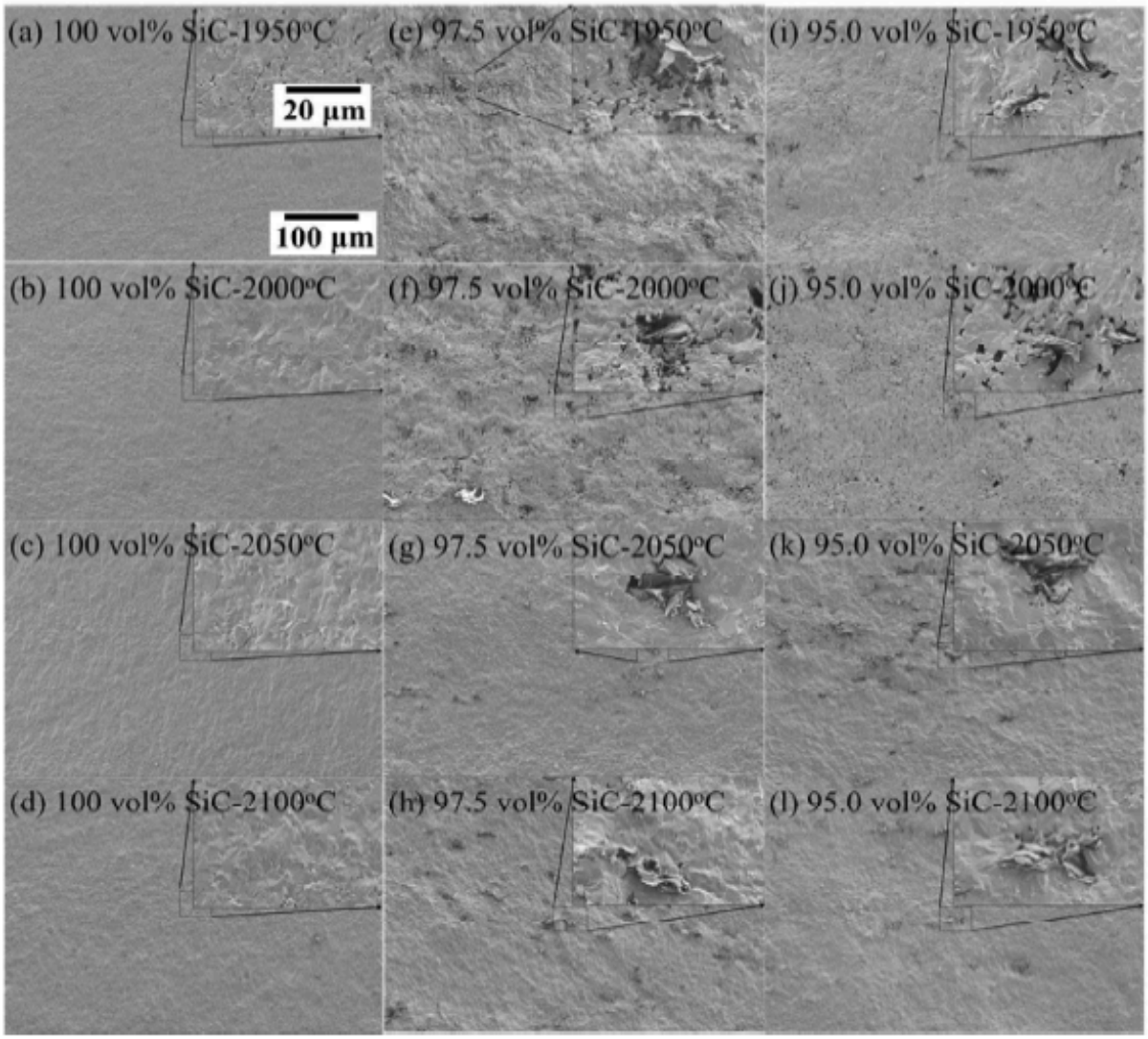

Fig. 3.3 SEM images of the fracture surfaces for the pure SiC and NFA-SiC composite samples at different sintering temperatures.

The fracture surface morphologies shown in Figs. 3.3 (e–h) for the 2.5 vol% NFA-97.5 vol% SiC samples and in Figs. 3.3 (i–l) for the 5.0 vol% NFA-95.0 vol% SiC samples deserve further discussion. For both compositions, some plate-like structures are present in the sintered matrix. As a matter of fact, the plate-like phase exhibits no difference among all the NFA-SiC samples. However, the structures around the plate-like structure show some differences at different sintering temperatures. As shown in Figs. 3.3 (e–f) and (i–j), at lower sintering temperatures of 1950°C and 2000°C, the 2.5 vol% NFA-97.5 vol% SiC and 5.0 vol% NFA-95.0 vol% SiC samples have porous structures around the plate-like structures. However, at higher sintering temperatures of 2050°C and 2100°C, the 2.5 vol% NFA-97.5 vol% SiC and 5.0 vol% NFA-95.0 vol% SiC samples have much denser structures, and the plate-like structures are tightly embedded in the matrix, as indicated in Figs. 3.3 (g–h) and (k–l).

When sintering the NFA-SiC composites, the reactions between NFA and SiC happen as follows: [38, 39, 66]

$$SiC \rightarrow Si + C \quad (3.1)$$

$$Fe + Si \rightarrow FeSi \quad (3.2)$$

$$Fe + 2Si \rightarrow FeSi_2 \quad (3.3)$$

$$3Fe + SiC \rightarrow Fe_3Si + 3C \quad (3.4)$$

$$3Fe + C \rightarrow Fe_3C \quad (3.5)$$

The Gibbs free energy of these reactions is shown in the table below[70, 71]. The unit of Gibbs free energy is kJ/mol. From the Gibbs free energy values shown in the table, iron silicides are most likely to be produced during the sintering process. The decomposition of SiC is difficult. However, the decomposition is possible when Fe enters the reaction.

Table 3.1 The Gibbs free energy of different reactions at 1950°C, 2000°C, 2050°C, and 2100°C.

Temperature/°C	SiC=>Si+C	Fe+Si=>FeSi	Fe+2Si=>$FeSi_2$	3Fe+SiC=>Fe_3Si+3C	3Fe+C=>Fe_3C
1950	53.68	-73.44	-60.52	-72.21	-12.85
2000	53.27	-73.44	-60.05	-73.34	-13.70
2050	52.87	-73.43	-59.59	-74.46	-14.56
2100	52.47	-73.43	-59.12	-75.59	-15.41

The plate-like structures shown in Fig. 3.3 should be related to the reaction products from the above equations. The elemental mapping images for the plate-like structures in the 5.0 vol% NFA-95.0 vol% SiC sample sintered at 2000°C are shown in Fig. 3.4. The plate-like area is identified as the carbon-rich phase, whereas elements Fe and Si are not observed in this area. Thus, this plate-like structure is formed of the carbon products from the decomposition of SiC [Eq. (1)], and the products of the reaction between Fe and SiC [Eq. (4)]. Other reaction products such as FeSi, $FeSi_2$ and Fe_3C around the plate-like structure further diffuse into the matrix from connected pores. The isolated Fe-rich domains are in the form of round shapes, with their sizes being around 1 μm. They are believed to be of FeSi, $FeSi_2$, and Fe_3C based on the equations (2–4). Due to the presence of dense local microstructures without any easy diffusion path, the Fe-rich phases are more likely to be isolated. This further demonstrates that the reaction products of the carbon-rich phases defer the densification process and lead to the formation of porous microstructures around them.

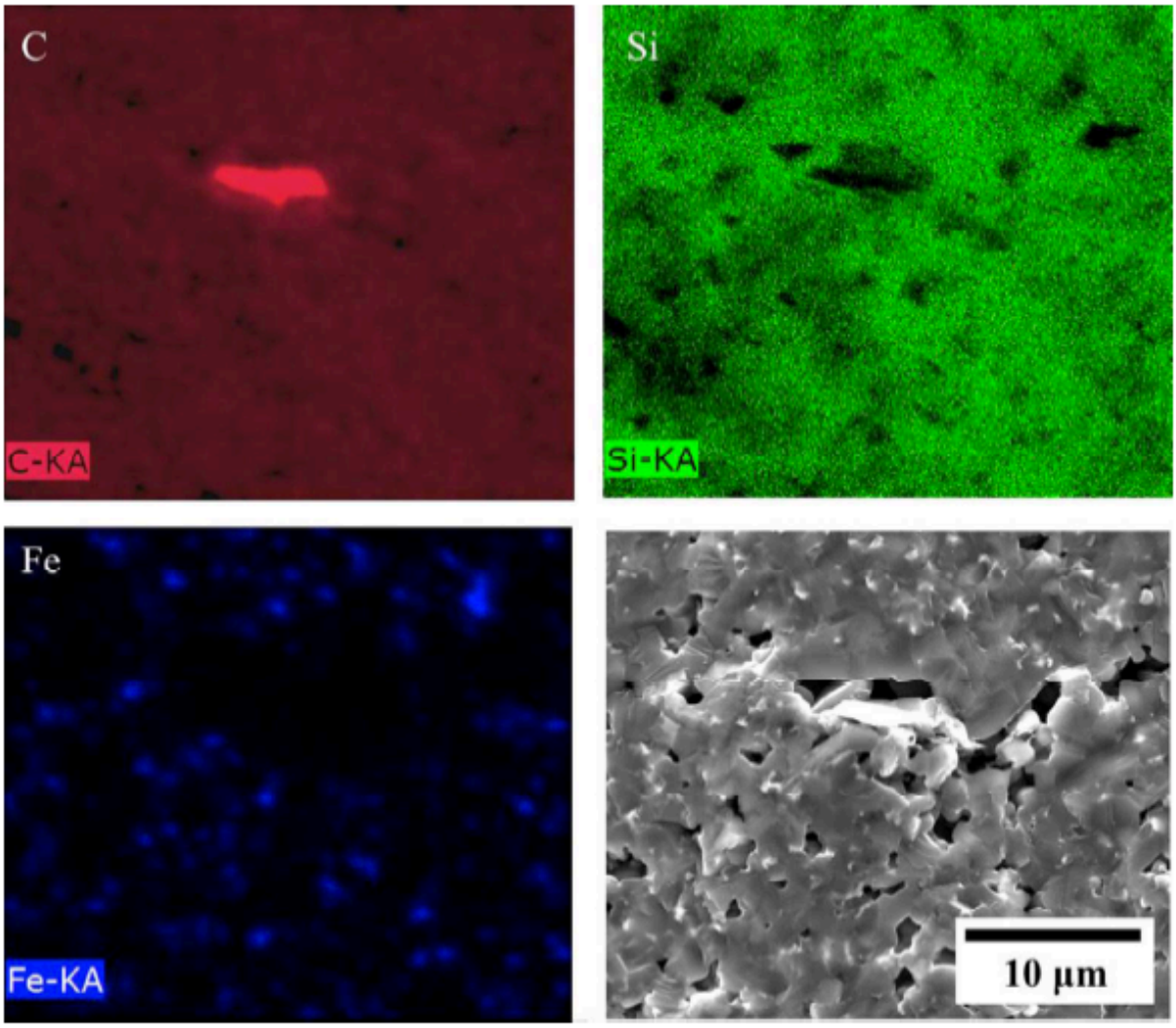

Fig. 3.4 Elemental mapping around the carbon-rich phase in the 5.0 vol% NFA-95.0 vol% SiC sample sintered at 2000°C.

3.3.4 Mechanical properties

Fig. 3.5 shows the Vickers hardness of the sintered pure SiC samples and NFA-SiC composite samples at four different sintering temperatures. The pure SiC samples have the highest hardness among all the samples at 1950°C–2100°C. The Vickers hardness has the increasing tendency with the values of 21.9±0.8 GPa at 1950°C, 24.0±0.7 GPa at 2000°C, 24.1±0.5 GPa at 2050°C, and 25.3±0.6 GPa at 2100°C.

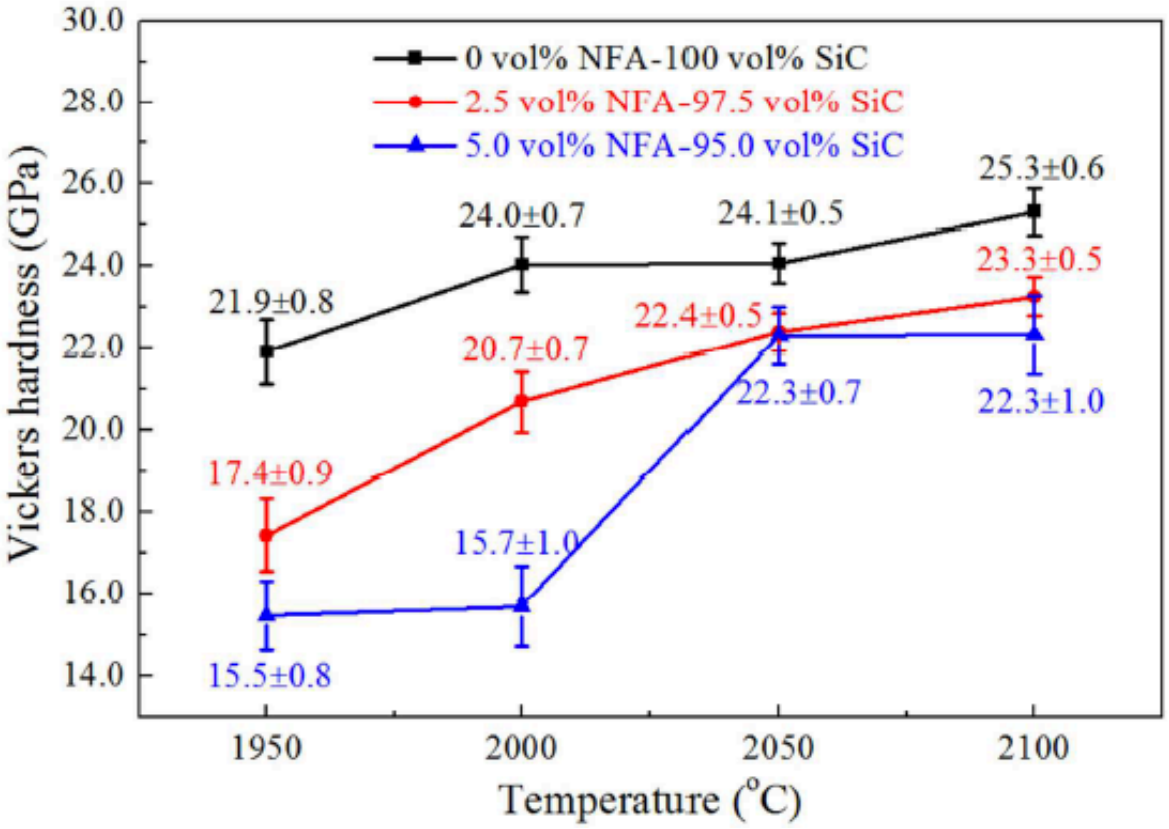

Fig. 3.5 Vickers hardness of the pure SiC and NFA-SiC composites at different sintering temperatures.

The 2.5 vol% NFA-97.5 vol% SiC samples have a slightly lower hardness than the pure SiC samples, but they still show a steadily increasing tendency of steady increase from 1950°C to 2100°C. Their Vickers hardness values are 17.4±0.9 GPa at 1950°C, 20.7±0.7 GPa at 2000°C, 22.4±0.5 GPa at 2050°C, and 23.3±0.5 GPa at 2100°C. With more NFA addition, the 5.0 vol% NFA-95.0 vol% SiC sample has lower Vickers hardness, especially at the sintering temperatures of 1950°C and 2000°C, with the corresponding values of 15.5±0.8 and 15.7±1.0 GPa, respectively. When the sintering temperature further increases to 2050°C, the Vickers hardness of the 5.0 vol% NFA-95.0 vol% SiC sample rapidly increases to 22.3±0.7 GPa, which is about the same as that of the 2.5 vol% NFA-97.5 vol% SiC sample. There is no continuing increase of the hardness when the sintering temperature increases to 2100°C.

The increasing tendency of the Vickers hardness for the pure SiC samples is consistent with the relative density change at different sintering temperatures. The Vickers hardness for the pure SiC sample reaches the maximum value of 25.3±0.6 GPa when the relative density reaches the maximum value of 99.0±0.1%. This means that the higher density enhances the hardness. The similar increasing tendency of the Vickers hardness with the increase in relative density has been demonstrated for the SPS sintered SiC [14]. The hardness

of the sintered pure SiC at 2100°C has the maximum value of 25.3±0.6 GPa, which is slightly higher than 25±0.2 GPa of the pure SiC sintered by SPS at 1800°C [14], but lower than 30±1 GPa of the pure SiC sintered under ultra-high pressure at 2200°C–2400°C [76]. The NFA addition samples have the maximum hardness value of 23.3±0.5 GPa at 2100°C, which is higher than 22.8±0.8 GPa of the hot pressed SiC [77] with Y_2O_3 and Al_2O_3 as additives at 1880°C, but is lower than 30.2±2.4 GPa of the pressureless sintered SiC at 2200°C with B_4C as an additive [78].

The lower Vickers hardness for the NFA-SiC composite samples can be understood as follows. The hardness of iron (4 GPa [79, 80]) is much lower than that of SiC (25-30 GPa [14, 76, 78]). Thus, for the NFA-SiC composites, the addition of even a small amount of NFA would lower their hardness. For the lower Vickers hardness of the 5.0 vol% NFA-95.0 vol% SiC samples vs. the 2.5 vol% NFA-97.5 vol% SiC samples at 1950°C and 2000°C, another reason should be considered. From the microstructures in Figs. 3.3 and 3.4, the NFA-SiC composites have porous structures around the carbon-rich phases; it is believed that these porous structures contribute to the lower hardness of the NFA-SiC composite samples. The higher NFA addition in the 5.0 vol% NFA-95.0 vol% SiC sample causes more porous structures, lower densities, and subsequently lower hardness than that of the 2.5 vol% NFA-97.5 vol% SiC sample.

However, the Vickers hardness of the 5.0 vol% NFA-95.0 vol% SiC samples is close to that of the 2.5 vol% NFA-97.5 vol% SiC samples at 2050°C and 2100°C. This is because at higher temperatures, the porous structures are greatly reduced and the matrix becomes much denser as compared to the samples sintered at lower temperatures, as indicated in Fig. 3.3. Although the densities for the 5.0 vol% NFA-95.0 vol% SiC samples are not as high as for the 2.5 vol% NFA-97.5 vol% SiC samples, the new phases compromise the Vickers hardness of the 5.0 vol% NFA-95.0 vol% SiC samples.

Fig. 3.6 shows two nano-indents on the 5.0 vol% NFA-95.0 vol% SiC sample sintered at 2100°C. The size of the indents is about 400 nm. The major elemental compositions for the matrix phase (Fig. 3.6a) and the bright phase (Fig. 3.6b) are listed in Table 3.2. The white phase contains high amounts of Fe and Cr. However, the matrix contains negligible amounts of such elements. Thus, the bright phase is probably the iron-rich phase of iron silicide/iron carbide that comes from the reaction between NFA and SiC. Furthermore, the nano-hardness measurements show that the bright phase has a smaller hardness value of 37.75 GPa, compared to 42.35 GPa for the matrix. Thus, the reaction products between SiC and NFA decrease the overall hardness of the NFA-SiC composite samples.

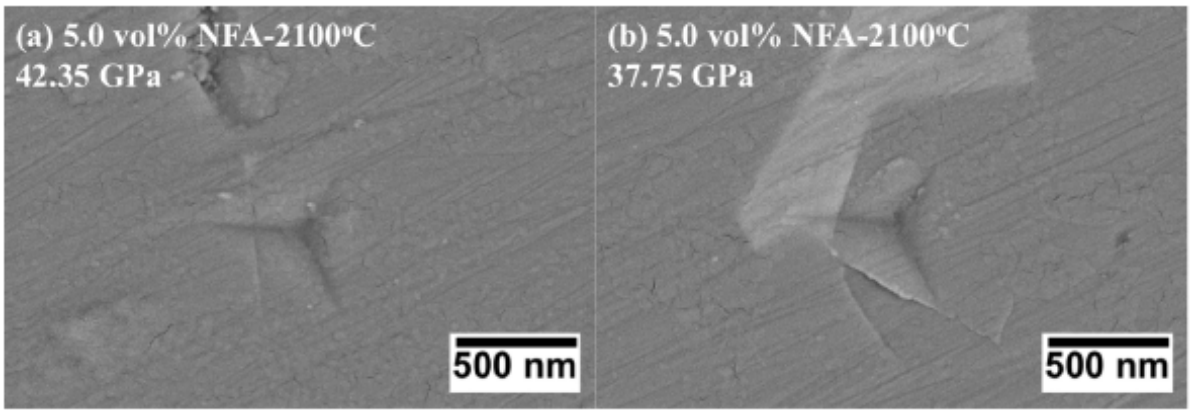

Fig. 3.6 SEM images of nano-indents for the 5.0 vol% NFA-95.0 vol% SiC sample sintered at 2100°C.

Table 3.2 Elemental compositions of the matrix phase and the bright phase (Fig. 6) in the 5.0 vol% NFA-95.0 vol% SiC sample sintered at 2100°C.

Elements	C/wt%	Si/wt%	Fe/wt%	Cr/wt%
Matrix phase	32.8±0.4	66.8±0.4	0.4±0.2	0
Bright phase	20.9±2.7	50.2±1.9	26.7±0.9	2.2±1.1

To assess the strength of the sintered SiC and NFA-SiC samples, the relation between flexural strength and Vickers hardness for SiC ceramics is obtained by a linear fitting of the literature data [81, 82, 83, 84, 85, 86, 87, 88], and can be expressed as follows:

$$\sigma_{FS} = 30.3H_v - 96.4 \quad (3.6)$$

where σ_{FS} is flexural strength, which has the unit of MPa; H_v is Vickers hardness, which has the unit of GPa. The specific information is in the supplemental information. Based on Eq. (6), the flexural strength of our sintered SiC and NFA-SiC composites is predicted as shown in Fig. 3.7. The change in the flexural strength is similar to that of the Vickers hardness as shown in Fig. 3.5. Higher sintering temperatures produce higher flexural strength for the SiC samples than for the NFA-SiC composites due to its higher Vickers hardness. Its highest flexural strength approaches 670±17 MPa at 2100°C, which is comparable to 652±33 GPa for hot pressed SiC ceramics using Al_2O_3 as an additive [88], and 691±12 GPa for hot pressed SiC ceramics using Al/B/C as additives [87]. For the NFA-SiC composite samples, the samples with the lower content of 2.5 vol% NFA have a higher flexural strength. The 2.5 vol% SiC-97.5

vol% and 5.0 vol% SiC-95.0 vol% samples reach their highest flexural strength of 608±16 MPa and 580±29 MPa at 2100°C, which are slightly lower than that of the pure SiC sample.

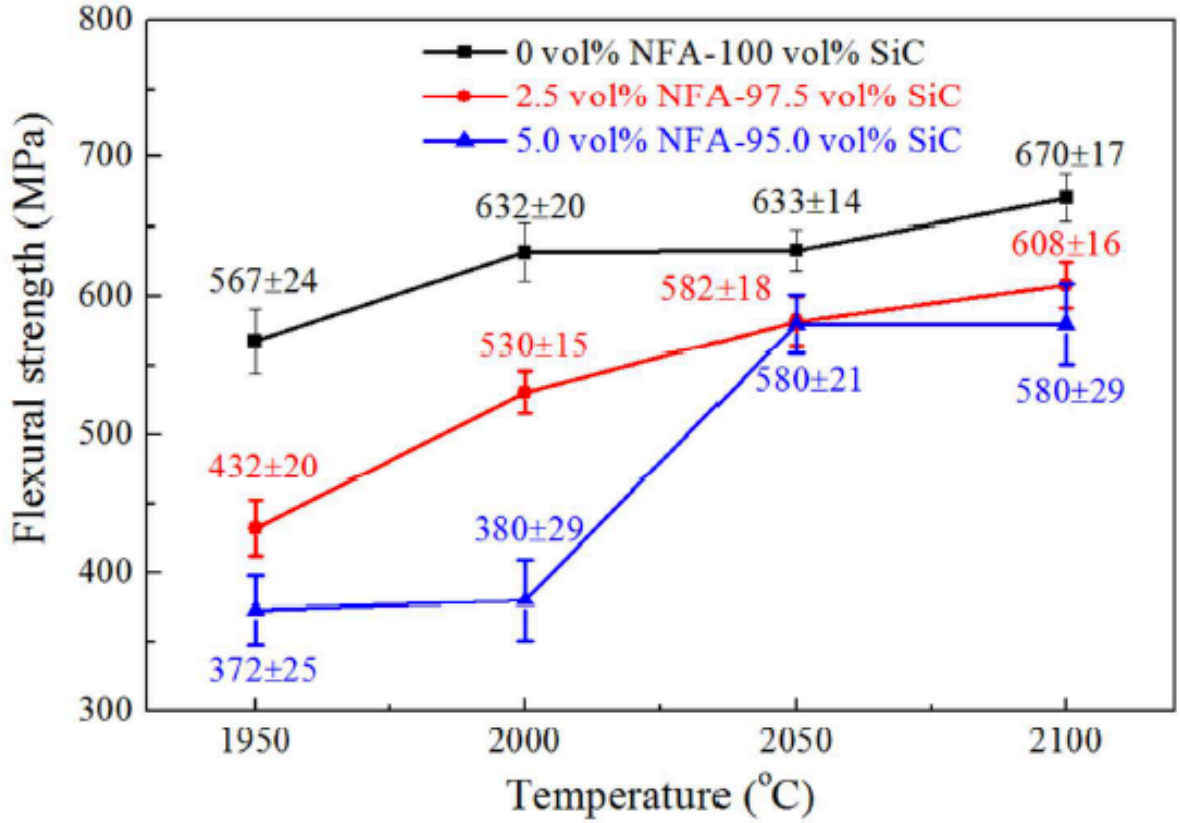

Fig. 3.7 Flexural strength of the pure SiC and NFA-SiC samples at different sintering temperatures.

3.4 Conclusions

Pure SiC and NFA-SiC composites with 2.5 vol% and 5.0 vol% NFA were sintered at 1950°C–2100°C by spark plasma sintering (SPS). The density of the pure SiC samples shows the increasing trend with the sintering temperature and reaches nearly full density at 2100°C. The 2.5 vol% NFA addition benefits the full densification of the NFA-SiC samples at the sintering temperature of 1950–2000°C, but slightly reduces the densification of the NFA-SiC samples at the sintering temperature of 2050–2100°C. The 5.0 vol% NFA-95.0 vol% SiC samples have the lowest density among all the samples. The NFA-SiC composites form lamellar phases of carbon-rich products which compromise the densification process. The Vickers hardness of the pure SiC and NFA-SiC composites increases with the sintering temperature in the range of 1950°C–2100°C. The estimated flexural strength for the pure SiC is higher than that for the NFA-SiC composites. The reactions between SiC and NFA

decrease the overall hardness of the NFA-SiC composites. The as-sintered SiC and NFA-SiC composites are promising cladding materials for nuclear applications.

4 Carbon coated NFA powders to prevent the reaction between NFA and SiC

4.1 Introduction

The NFA-SiC composites are expected to be a remarkable candidate for being nuclear cladding material. However, reaction between Fe (the base element of NFA) and SiC is known to happen during the fabrication of Fe-SiC composite, both in experiment [38, 39, 66] and in simulation [89]. The process starts with the decomposition of SiC. The decomposed Si and C then easily interact with Fe and form silicides (e.g. Fe_3Si, FeSi and $FeSi_2$) and carbides (e.g. Fe_3C). For example, Pelleg[39] produced Fe-SiC composites using sintering and hot isostatic pressing (HIP) in the temperature range of 900°C to 1100°C, finding a large amount of pearlite and iron silicides. Shen et al.[66] confirmed that several products, such as Fe_3C (a component of the pearlite), Fe (Si), Fe_3Si, Fe_2Si, and C, come from different reactions between Fe and SiC. Therefore, to successfully fabricate SiC-NFA composites, excessive reactions between NFA and SiC should be prevented.

Considering this problem, one possibility to achieve high density SiC ceramics with NFA as an additive is by the fast sintering of SPS to decrease the potential reactions between them. The other way to reduce/avoid the interaction between SiC and NFA, by applying a carbon coating on NFA, shows promise. This is because carbon does not react with silicon carbide, and the solubility of carbon in Fe is very small. So the existence of carbon will prevent the reaction between NFA and SiC by forming a barrier. What is more, even though iron carbide is formed after sintering, the iron carbide layer can still prevent the reaction. Moreover, the thin carbon layer only consumes a small amount of NFA. In this study, carbon coating on NFA was used to prevent the reaction between SiC and NFA. The carbon coating is effective up to 1250°C, and the coating film quality is examined by SEM. The carbon film is uniform with thickness of 800 nm.

4.2 Experimental Procedures

4.2.1 Coating NFA powders with sucrose

First, sucrose ($C_{12}H_{22}O_{11}$, 99%, Alfa Aesar, Ward Hill, MA) was dissolved into ethanol (C_2H_5OH, Decon Laboratories, Inc., King of Prussia, PA). Then, NFA powders were poured into the ethanol solution. After that, the ethanol solution with NFA powders was heated on a hot plate to 60^{o}C. At the same time, the ethanol solution was stirred to make sure that the sucrose was uniformly deposited on the surface of NFA powders during the evaporation process. After the ethanol solution dried, the NFA powders were ground to make them more uniform with the coating film. The molar ratio of Fe and C was controlled at 4:1.

4.2.2 Coating NFA powders with carbon

To convert the sucrose, on the surface of the NFA powders, into carbon, the NFA powders were thermally treated at 400^{o}C for 1 hour in Ar atmosphere. The heating rate was controlled at 5^{o}C/min. The sucrose decomposed at this temperature, and only carbon was left on the surface of NFA powders during the treatment.

4.2.3 Preparing NFA-SiC composites

The carbon coated NFA powders were mixed with SiC powders by grinding the mixture in a mortar for 20 minutes. Then the mixed powders were cold pressed at 15,000 psi for 5 minutes. The pressed samples were cylinders with 12.7 mm diameter and 4 mm thickness. The volume ratio between NFA and SiC were controlled at 9:1 and 7:3. The green samples were then sintered in a furnace in Ar atmosphere. The peak temperatures were 850^{o}C, 1050^{o}C, and 1250^{o}C, and the holding time was 1 hour.

4.2.4 Testing the reaction by XRD

The coated NFA powders were mounted in epoxy and then carefully polished to examine the cross-section of the coated powders. The quality and thickness of the carbon coating film were examined by scanning electron microscopy (FEI FEG-ESEM Quanta600, FEI Company, Hillsboro, OR, USA). The sintered NFA-SiC samples were examined by X-ray diffraction (XRD, PANalytical B. V., Almelo, Netherlands).

4.3 Results and Discussion

4.3.1 SEM of carbon coating film

Fig. 4.1 and Fig. 4.2 show the carbon coating film on NFA particles. As shown in Fig. 4.1, the carbon coating film is very uniform around the round NFA powders. In addition, both large and small powders have the good quality carbon coating film. In Fig. 4.2, the high magnification SEM image clearly shows the thickness of the carbon coating. The thickness of the film is around 800 nm.

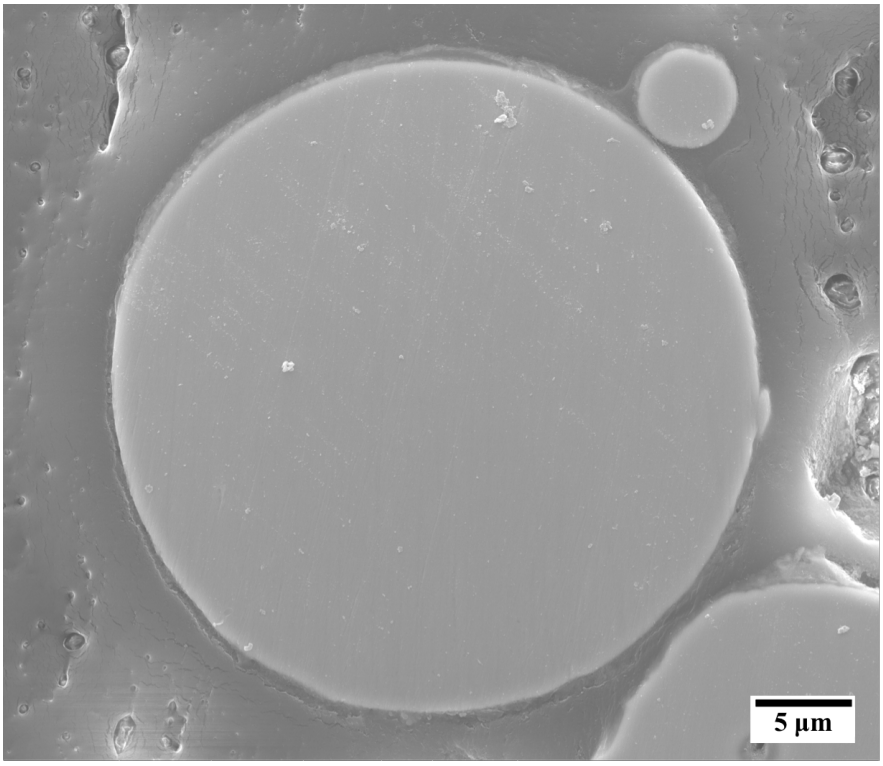

Fig. 4.1 SEM images of the cross-section of carbon coated NFA powders.

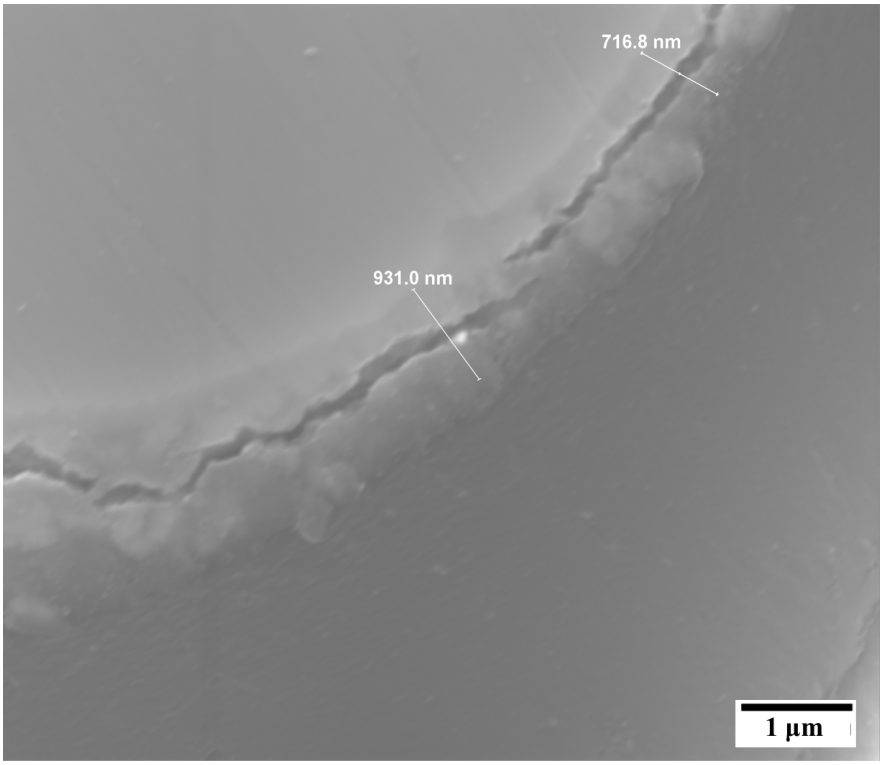

Fig. 4.2 Thickness of the carbon coated film.

4.3.2 Effectiveness of carbon coating

Fig. 4.3 and Fig. 4.4 show the XRD pattern of sintered carbon coated NFA-SiC composites with 90 vol% NFA-10 vol% SiC and 70 vol% NFA-30 vol% SiC compositions at 850^{o}C, 1050^{o}C, and 1250^{o}C sintering temperatures. For both compositions, there are no peaks detected from iron silicides at 850^{o}C and 1050^{o}C sintering temperatures. The peaks from SiC and NFA are clearly presented in the XRD patterns. This means that the carbon coating is effective in preventing the reaction between NFA and SiC by forming a contact barrier. However, at the sintering temperature of 1250^{o}C, reaction occurs. In Fig. 4.4, the peaks from Fe_3Si are detected in the XRD pattern. In addition, no peaks from SiC are detected, which means that the SiC has reacted with NFA, with a little SiC is being left behind. This is because at temperatures closer to the melting point of NFA, in the range of 1400–1500^{o}C, such as at 1250^{o}C, the NFA powders become more active. During the Fe diffusion process, the carbon coating film might be broken, and the NFA powders come into contact with SiC. In this case, the carbon coating stops working. In Fig. 4.3, there is no peak from Fe_3Si; this might be due to the small amount of SiC in the composite. In this case, most of the NFA stays in the form of Fe instead of Fe_3Si, and so the peaks of Fe_3Si are not presented in the XRD pattern.

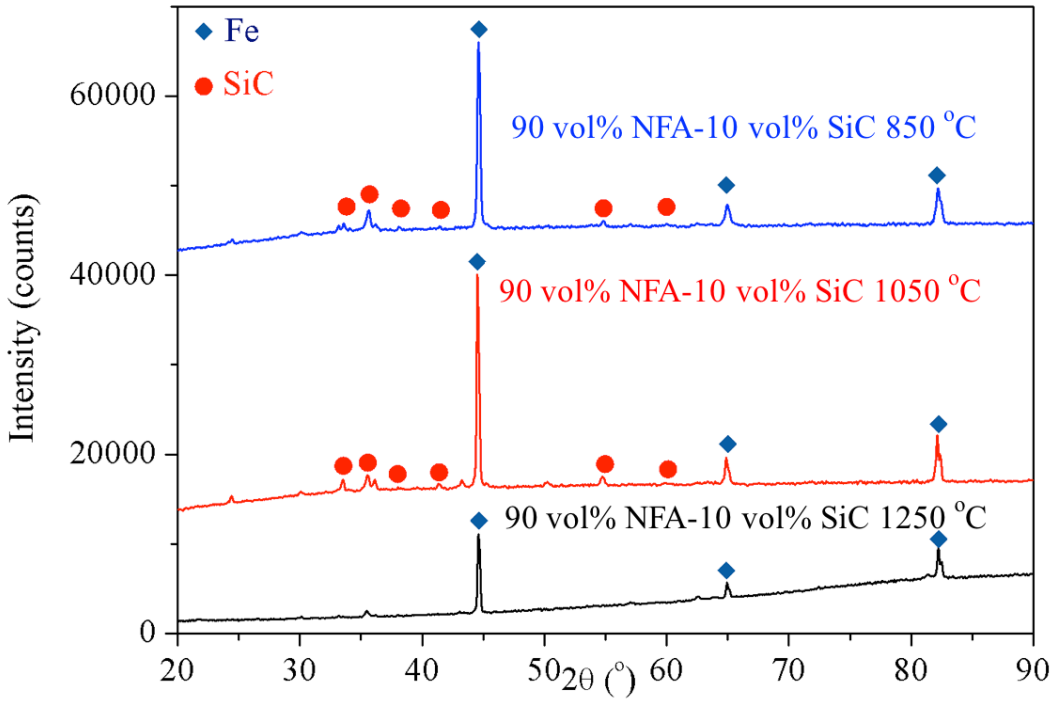

Fig. 4.3 XRD pattern of 90 vol% C coated NFA-10 vol% SiC sintered at 850°C, 1050°C, and 1250°C for 1 hour.

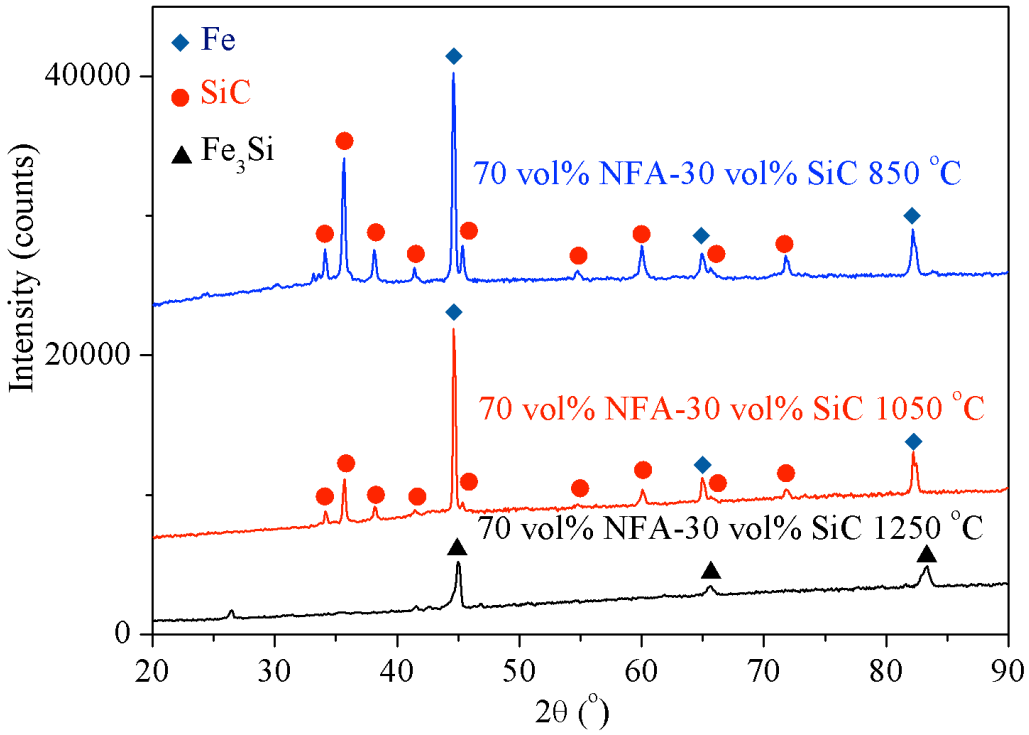

Fig. 4.4 XRD pattern of 70 vol% C coated NFA-30 vol% SiC sintered at 850°C, 1050°C, and 1250°C for 1 hour.

4.4 Conclusions

The surface of NFA powders was successfully coated with a uniform carbon film through the evaporation of sucrose ethanol solution. The thickness of the carbon film is around 800 nm. The carbon coating can effectively prevent the reaction between NFA and SiC except for very high sintering temperatures. At a very high temperature (1250^{o}C), the NFA powders melt and are leaked from the carbon film.

4.5 Problems and future works

The evidence of the presence of the carbon layer is only in the SEM images, and so, the evidence is not very solid. Since the NFA particles are mounted in the epoxy, which contains lots of carbon elements, it is difficult to differentiate between the carbon layer and epoxy by EDS. To get a solid evidence of the presence of the carbon layer, cutting the coated NFA particles by Focused Ion Beam (FIB) is a good method. This is because, there will not be any epoxy that interferes with the results. As a result, the carbon layer and NFA particles can be differentiated by EDS or backscattered electron images.

According to the results, the reaction can only be stopped by 1050^{o}C. It does not affect the sintering of high content NFA composite, because 1050^{o}C is high enough. However, high content SiC composites, such as 30 vol% NFA- 70 vol% SiC, need higher sintering temperature to achieve full density. The carbon coating will not work at that time. In the future, a better coating should be studied to solve this problem.

5 Fabrication of gradient-structured NFA-SiC composites

5.1 Introduction

The ultimate objective is fabricating a gradient-structured NFA-SiC core material by utilizing the advantage of NFA—great radiation resistance, and the advantages of SiC—great mechanical property and chemical stability. Near the nuclear reactor, pure NFA is designed for resisting radiation; on the far end of the nuclear reactor, pure SiC is designed to strengthen the whole core material. Between the pure NFA and the pure SiC, the gradient-structured NFA-SiC composites are required. So, the properties of NFA and SiC will gradually change along with the changes in composition.

In this chapter, slip casting of the co-suspension of NFA and SiC was used to fabricate the gradient-structured NFA-SiC composites. The viscosity properties of the co-suspension were studied, and the green gradient-structured samples were successfully fabricated.

5.2 Experimental procedure

Commercial SiC particles (ABCR GmbH & Co.KG, SiC UF-15 Silicon Carbide Grade UF-15 - A product of H. C. Starck) and lab-made NFA particles (from Dr. T. S. Byun of PNNL) were used for this procedure. NFA particles were screened with a mesh size of No. 635 (20 μm). HORIBA laser light scattering particle size distribution analyzer was used to analyze particle size and particle size distribution of SiC and NFA.

Suspensions of SiC and NFA mixtures were prepared by ball milling mixed particles in water. The NFA makes up 0, 3, 15, 20, 25, 30, 40, 45, 50, 55, 60, and 70 vol% of total solids (NFA and SiC). For all the suspensions, the SiC solids loading was controlled at 40 vol%; the NFA contents were adjusted accordingly. Poly (acrylic acid) (PAA, Sigma-Aldrich, St. Louis, MO), with an average molecular weight of 2000 and 0.2 wt% concentration (in water), was used as a dispersant. SiC particles were added into water (with the initial pH value at 11, adjusted using dilute ammonium hydroxide) along with 0.2 wt% PAA dispersant (on SiC basis); the suspension was ball milled for 20 min. The solids loading of NFA-SiC co-suspension was controlled at 43 vol%. The solids loading of pure SiC suspension were controlled at 40 vol%. The viscosity measurements of the suspensions were performed using a rheometer with a cone-plate geometry (AR 2000; TA Instruments, New Castle, DE).

PDMS prepolymer (Sylgard 184, Dow Corning, Midland, MI) with base and curing agents at 10:1 ratio was cast on a steel disk with 25 mm diameter and 1.8 mm thickness. The steel and PDMS prepolymer were placed in a vacuum chamber for 60 min to remove air bubbles, and then placed in an oven at 100^{o}C for 60 min to solidify the PDMS molds.

The SiC and NFA mixture particle suspension was poured and cast into the PDMS molds using a pipette. Care was taken to ensure that the suspension flowed into and completely filled the molds. The filled molds were put into a petri dish to dry under ambient conditions for 7 days. To maintain the humidity inside the petri dish during drying and to avoid its cracking, 1 mL of water was added to the petri dish. After the samples were dried, they were carefully separated from the PDMS molds. Single composition samples with 0, 3, 15, 20, 25, 30, 40, 45, 50, 55, 60, and 70 vol% NFAs were successfully made. And samples with layer structures (gradient compositions) were also successfully made, including three layers (Pure SiC-30vol% NFA-60vol% NFA), four layers (Pure SiC-20vol% NFA-40vol% NFA-60vol% NFA), and five layers (Pure SiC-15vol% NFA-30vol% NFA-45vol% NFA-60vol% NFA).

The microstructure of green samples were characterized by optical microscopy (OM, BH-2; Olympus).

5.3 Results and Discussion

5.3.1 Particle size and distribution

Fig. 5.1 and Fig. 5.2 show the particle size and distribution of SiC and NFA respectively. The black line gives the information of particle size distribution, and the blue line gives the information of cumulative particle size distribution. The SiC particles show the mean size of 1.24 μm, median size of 0.71 μm, and mode size of 0.55 μm. The NFA particles show the mean size of 14.28 μm, median size of 14.57 μm, and the mode size of 16.03 μm.

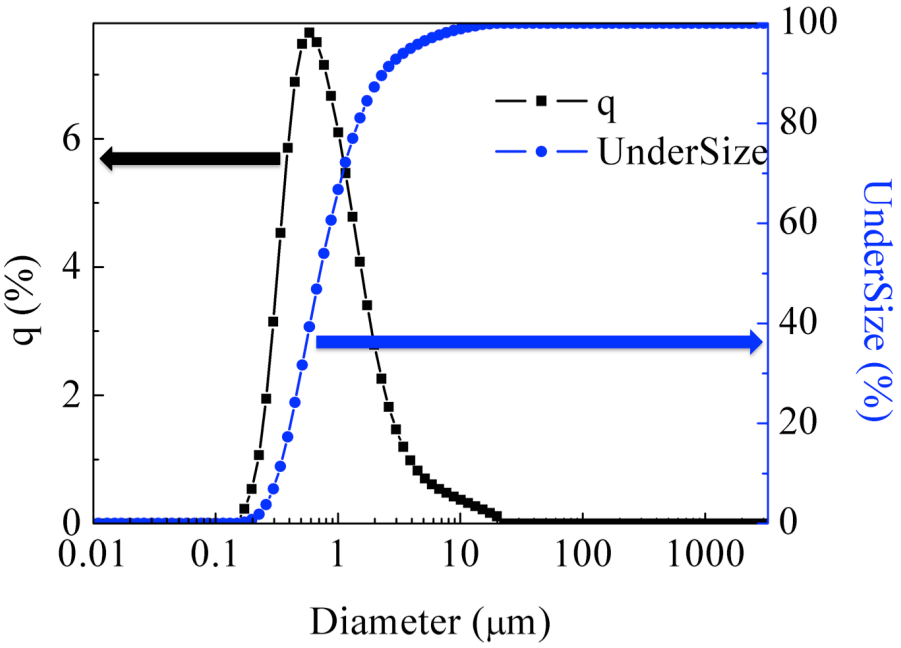

Fig. 5.1 Particle size and distribution of as-received SiC particles.

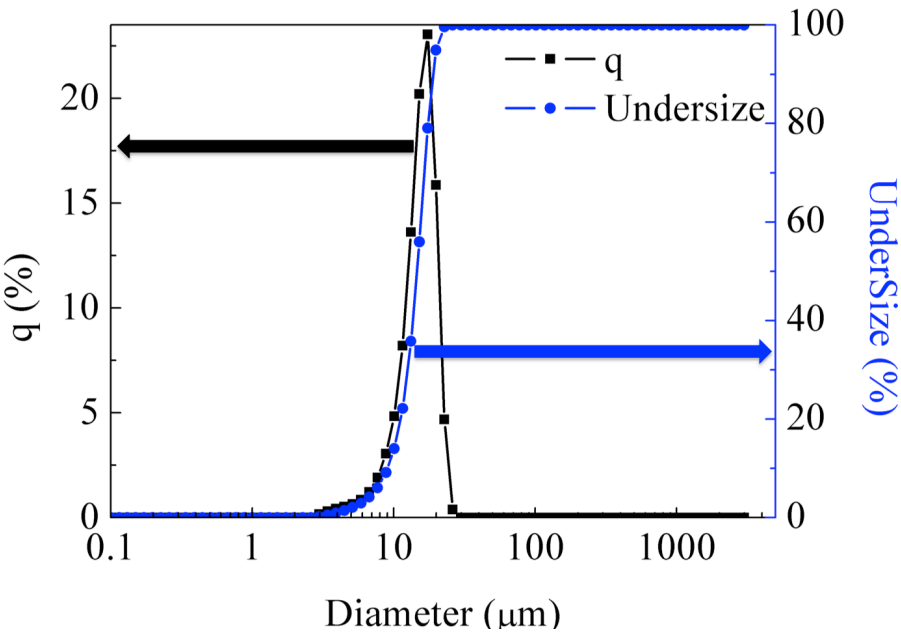

Fig. 5.2 Particle size and distribution of NFA particles.

5.3.2 Viscosity of NFA-SiC co-suspension

Fig. 5.3 shows the viscosity of pure SiC and NFA-SiC co-suspension. Due to the large particle size of NFA particles, it was impossible to make a pure NFA water-based suspension. The NFA particles were deposited too soon, and the pure NFA suspension was unstable. However, dispersing NFA particles in the SiC suspension is stable. Because the SiC suspension has enough viscosity to hold NFA particles, NFA would not be deposited at the bottom of the suspension. The solids loading of NFA-SiC co-suspension is set as 43 vol%.

The solids loading of pure SiC suspension is 40 vol%, because the highest solid loading that pure SiC suspension can achieve is 40 vol%.

The volume percent shown in the figure is the concentration of NFA in the solids (NFA and SiC). For example, the 25 vol% NFA suspension means that the solids consist of 25 vol% NFA and 75 vol% SiC. From the figure, 50 vol% NFAs-50 vol% SiC has the lowest viscosity. Regardless of whether the concentration of NFA is higher or lower, the viscosity of the co-suspension increases. In addition, the highest concentration that the NFA particles can be stably dispersed in is 70 vol%.

When the solid loading is set as 43 vol%, the 50 vol% NFA-50 vol% SiC co-suspension has the lowest viscosity. This can be explained as follows. The SiC particles have a much smaller particle size (1.24 μm) than the NFA particles (14.28 μm). Compared with the pure suspension, the co-suspension contains two kinds of particles with different particle sizes. The smaller SiC particles are dispersed in the interspace of the larger NFA particles. In other words, the particles in the co-suspension have a better stacking than that of the pure suspension. So at the same solid loading, the particles in the co-suspension are much easier to move around than the particles in the pure suspension. The highest solid loading that pure SiC suspension can achieve is 40 vol%. After adding some NFA particles, such as 12.5 vol% NFA-87.5 vol% SiC, a higher solid loading of 43 vol% can be achieved. This also confirms the explanation above.

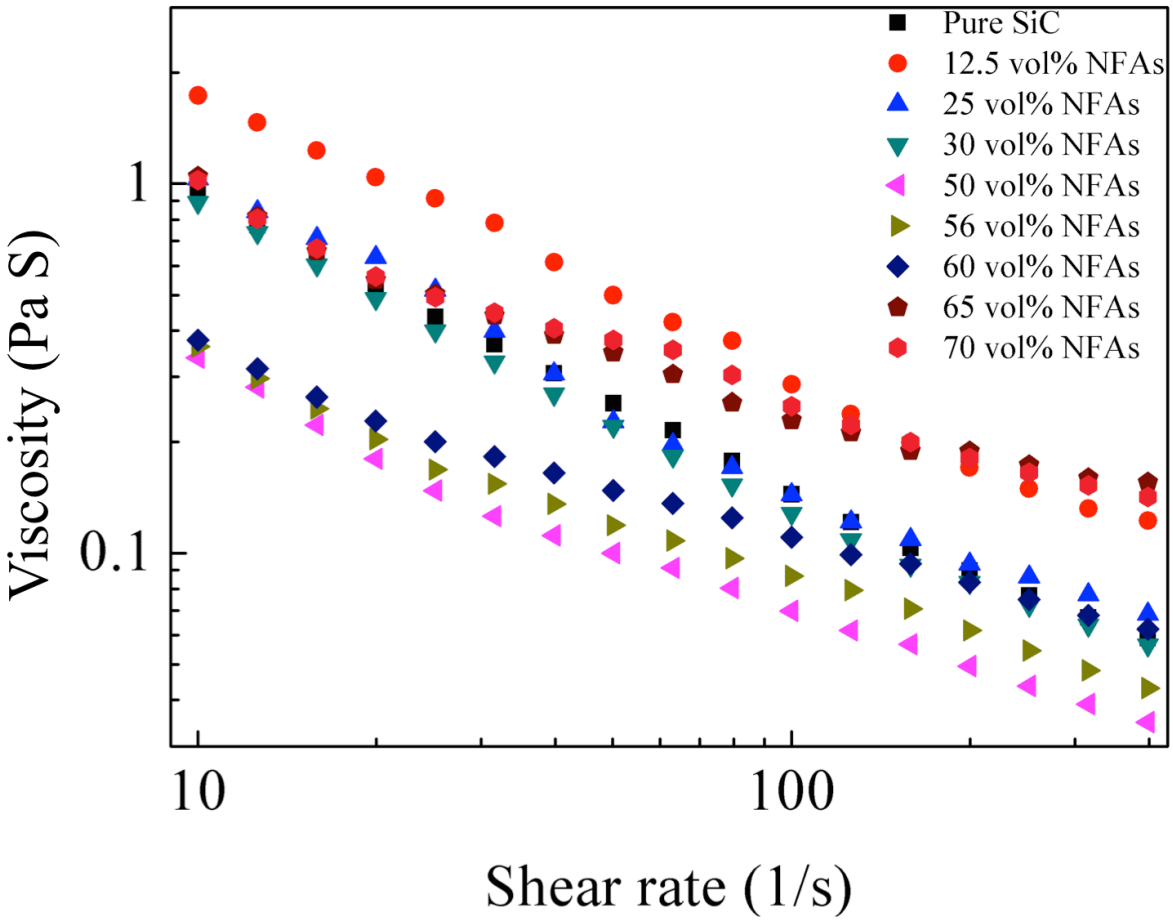

Fig. 5.3 Viscosity of pure NFA and NFA-SiC co-suspension.

5.3.3 Microstructure of gradient-structured green samples

Fig. 5.4 to Fig. 5.9 show the cross-section optical images of the gradient-structured NFA-SiC composites. Fig. 5.4 shows the 3 layers gradient-structured NFA-SiC composites, and the 3 layers are pure SiC, 25 vol% NFA-75 vol% SiC, and 50 vol% NFA-50 vol% SiC. Fig. 5.5 shows the 3 layers of the gradient-structured NFA-SiC composites, and the 3 layers are pure SiC, 30 vol% NFA-70 vol% SiC, and 60 vol% NFA-40 vol% SiC. Fig. 5.6 shows the 4 layers of gradient-structured NFA-SiC composites, and the 4 layers are pure SiC, 20 vol% NFA-80 vol% SiC, 40 vol% NFA-60 vol% SiC, and 60 vol% NFA-40 vol% SiC. Fig. 5.7 shows the 4 layers of gradient-structured NFA-SiC composites, and the 4 layers are pure SiC, 25 vol% NFA-75 vol% SiC, 45 vol% NFA-55 vol% SiC, and 65 vol% NFA-35 vol% SiC. Fig. 5.8 shows the 5 layers of gradient-structured NFA-SiC composites, and the 5 layers are pure SiC, 15 vol% NFA-85 vol% SiC, 30 vol% NFA-70 vol% SiC, 45 vol% NFA-55 vol% SiC, and 60 vol% NFA-40 vol% SiC. Fig. 5.9 shows the 5 layers of gradient-structured NFA-SiC composites, and the 5 layers are pure SiC, 25 vol% NFA-75 vol% SiC, 40 vol% NFA-60 vol% SiC, 55 vol% NFA-45 vol% SiC, and 70 vol% NFA-30 vol% SiC.

All the six samples show that the gradient-structured samples were successfully made. Distribution of NFA powders in each layer is uniform and the boundary between different layers is clear.

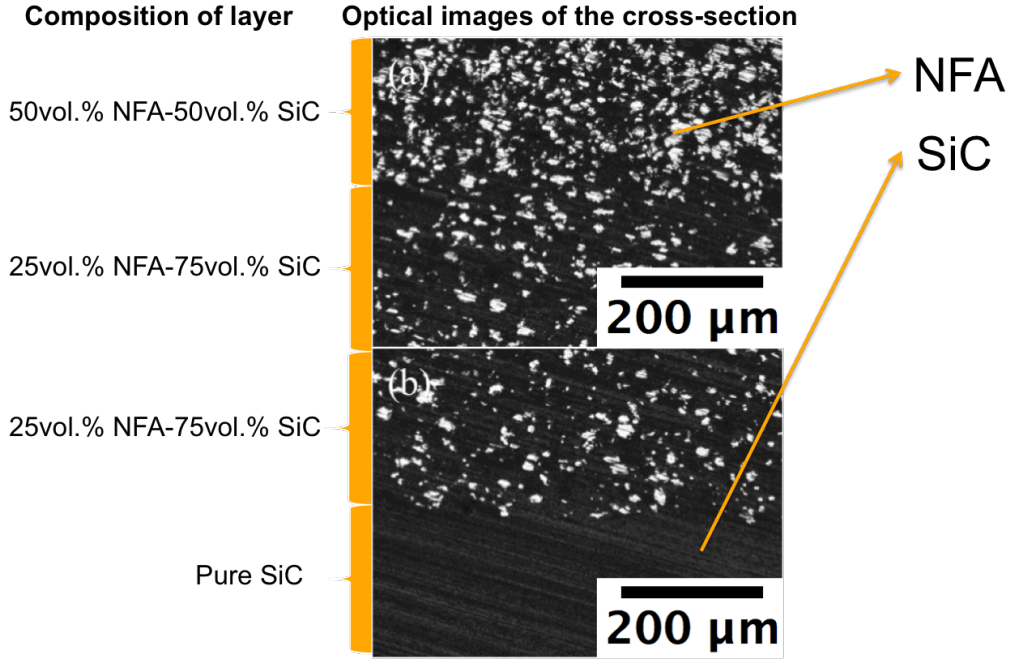

Fig. 5.4 Cross-section optical images of 50 vol% NFA-50 vol% SiC, 25 vol% NFA-75 vol% SiC, and pure SiC gradient-structured NFA-SiC composites.

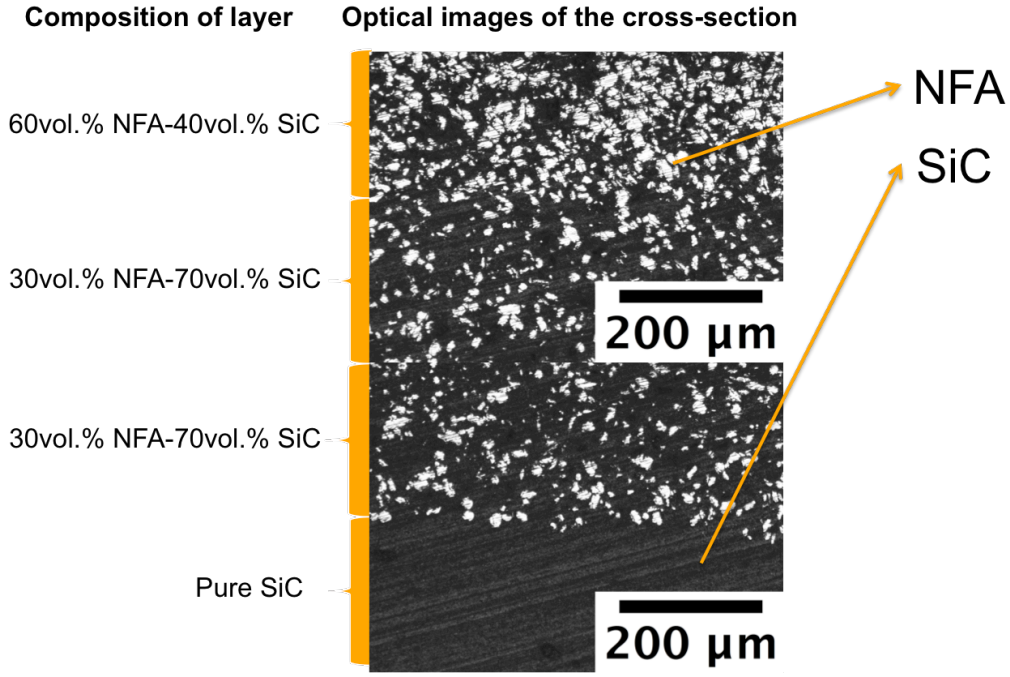

Fig. 5.5 Cross-section optical images of 60 vol% NFA-40 vol% SiC, 30 vol% NFA-70 vol% SiC, and pure SiC gradient-structured NFA-SiC composites.

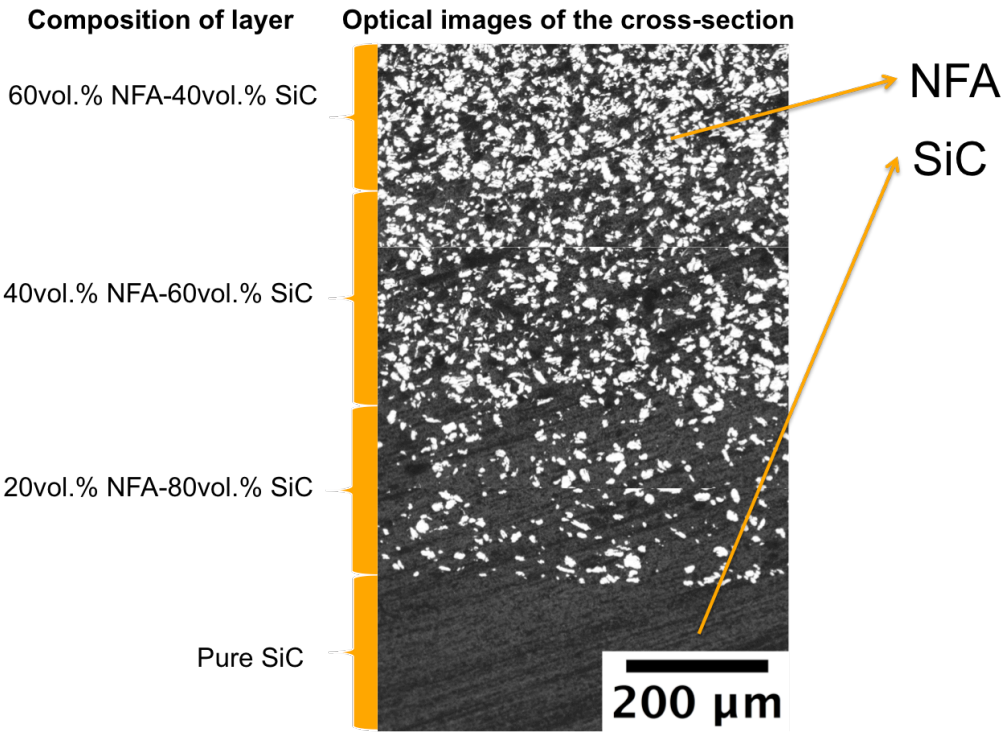

Fig. 5.6 Cross-section optical images of 60 vol% NFA-40 vol% SiC, 40 vol% NFA-60 vol% SiC, 20 vol% NFA-80 vol% SiC, and pure SiC gradient-structured NFA-SiC composites.

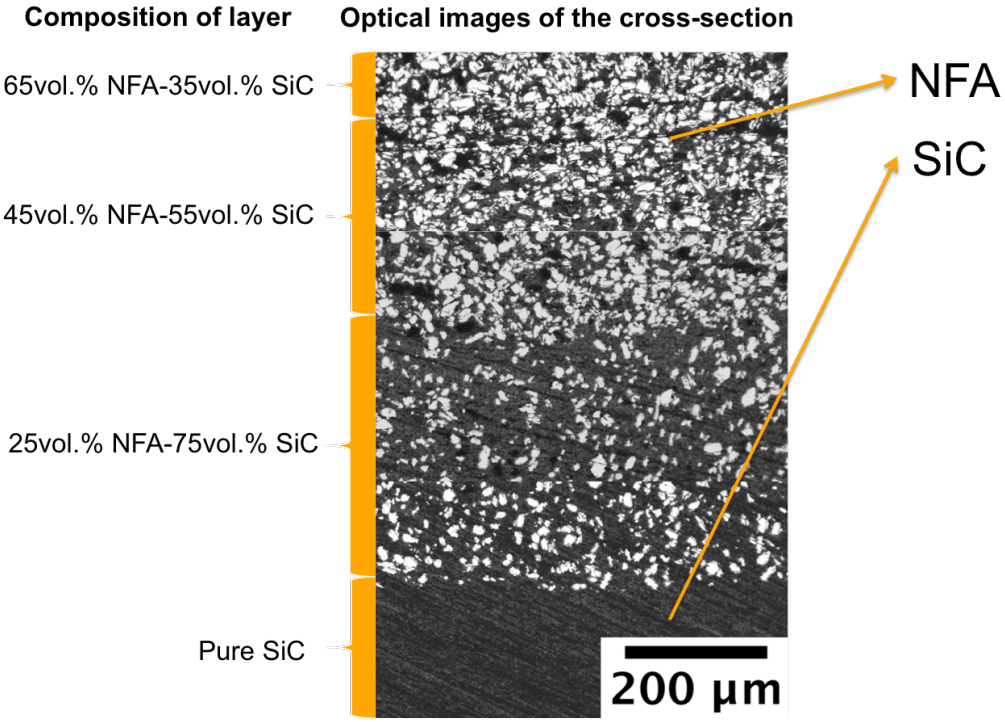

Fig. 5.7 Cross-section optical images of 65 vol% NFA-35 vol% SiC, 45 vol% NFA-55 vol% SiC, 25 vol% NFA-75 vol% SiC, and pure SiC gradient-structured NFA-SiC composites.

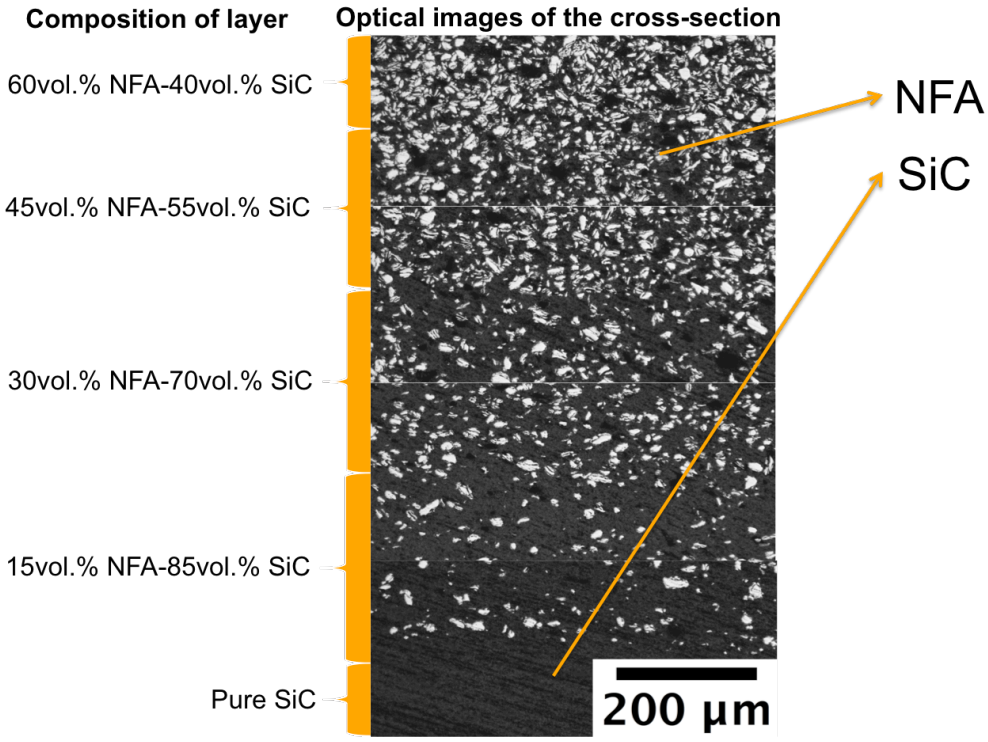

Fig. 5.8 Cross-section optical images of 60 vol% NFA-40 vol% SiC, 45 vol% NFA-55 vol% SiC, 30 vol% NFA-70 vol% SiC, 15 vol% NFA-85 vol% SiC, and pure SiC gradient-structured NFA-SiC composites.

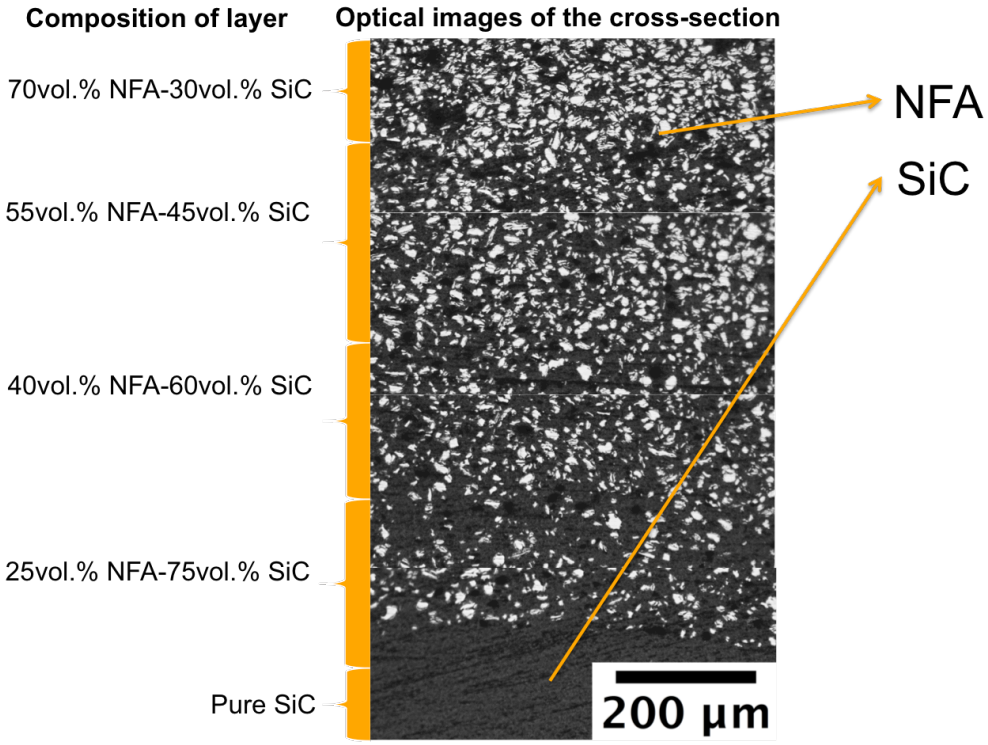

Fig. 5.9 Cross-section optical images of 70 vol% NFA-30 vol% SiC, 55 vol% NFA-45 vol% SiC, 40 vol% NFA-60 vol% SiC, 25 vol% NFA-75 vol% SiC, and pure SiC gradient-structured NFA-SiC composites.

5.4 Conclusion

In this chapter, different gradient-structured NFA-SiC green samples were successfully fabricated, and the viscosity properties of NFA-SiC co-suspension were studied. The 50 vol% NFA-50 vol% SiC co-suspension showed the lowest viscosity. And 70 vol% NFA-30 vol% SiC is the highest NFA concentration in which a stable co-suspension can be made. Due to the large difference between the melting point of NFA (~1500^{o}C) and SiC (2730^{o}C), the sintering of the gradient-structured NFA-SiC samples would be complicated. So the sintering conditions for the gradient-structured NFA-SiC samples should be studied and optimized.

5.5 Future work

In the future, the sintering work should be conducted. As discussed above, the sintering of the gradient-structured NFA-SiC samples would be complicated due to their complicated structures and the large difference in melting points. So the sintering conditions for different samples will be optimized, and the effects of the different sintering conditions will be studied.

References

1. T. S. Byun, J. H. Yoon, D. T. Hoelzer, Y. B. Lee, S. H. Kang, and S. A. Maloy, "Process development for 9Cr nanostructured ferritic alloy (NFA) with high fracture toughness," *J Nucl Mater,* 449[1-3] 290-99 (2014).

2. T. S. Byun, J. H. Yoon, S. H. Wee, D. T. Hoelzer, and S. A. Maloy, "Fracture behavior of 9Cr nanostructured ferritic alloy with improved fracture toughness," *J Nucl Mater,* 449[1-3] 39-48 (2014).

3. M. F. Ashby, "Materials selection in mechanical design,″ pp. xv, 646 p. 4th ed. Butterworth-Heinemann: Burlington, MA, (2011).

4. Y. Katoh, K. Ozawa, C. Shih, T. Nozawa, R. J. Shinavski, A. Hasegawa, and L. L. Snead, "Continuous SiC fiber, CVI SiC matrix composites for nuclear applications: Properties and irradiation effects," *J Nucl Mater,* 448[1-3] 448-76 (2014).

5. L. L. Snead, T. Nozawa, M. Ferraris, Y. Katoh, R. Shinavski, and M. Sawan, "Silicon carbide composites as fusion power reactor structural materials," *J Nucl Mater,* 417[1-3] 330-39 (2011).

6. L. Giancarli, H. Golfier, S. Nishio, R. Raffray, C. Wong, and R. Yamada, "Progress in blanket designs using SiCf/SiC composites," *Fusion Eng Des,* 61-62 307-18 (2002).

7. Y. Katoh, L. L. Snead, I. Szlufarska, and W. J. Weber, "Radiation effects in SiC for nuclear structural applications," *Curr Opin Solid St M,* 16[3] 143-52 (2012).

8. G. R. Desiraju and J. Hulliger, "Current opinion in solid state & materials science molecular crystals and materials," *Curr Opin Solid St M,* 5[2-3] 105-06 (2001).

9. K. Fukuda and K. Iwamoto, "Diffusion Behavior of Fission-Product in Pyrolytic Silicon-Carbide," *J Nucl Mater,* 75[1] 131-44 (1978).

10. W. Schenk and H. Nabielek, "High-Temperature Reactor-Fuel Fission-Product Release and Distribution at 1600-Degrees-C to 1800-Degrees-C," *Nucl Technol,* 96[3] 323-36 (1991).

11. Y. W. Kim, M. Mitomo, H. Emoto, and J. G. Lee, "Effect of initial alpha-phase content on microstructure and mechanical properties of sintered silicon carbide," *J Am Ceram Soc,* 81[12] 3136-40 (1998).

12. M. Hotta, H. Kita, and J. Hojo, "Nanostructured silicon carbide ceramics fabricated through liquid-phase sintering by spark plasma sintering," *J Ceram Soc Jpn,* 119[1386] 129-32 (2011).

13. C. Lorrette, A. Reau, and L. Briottet, "Mechanical properties of nanostructured silicon carbide consolidated by spark plasma sintering," *J Eur Ceram Soc,* 33[1] 147-56 (2013).

14. F. Lomello, G. Bonnefont, Y. Leconte, N. Herlin-Boime, and G. Fantozzi, "Processing of nano-SiC ceramics: Densification by SPS and mechanical characterization," *J Eur Ceram Soc,* 32[3] 633-41 (2012).

15. H. Tanaka, "Silicon carbide powder and sintered materials," *J Ceram Soc Jpn,* 119[1387] 218-33 (2011).

16. J. H. She and K. Ueno, "Effect of additive content on liquid-phase sintering on silicon carbide ceramics," *Materials Research Bulletin,* 34[10–11] 1629-36 (1999).

17. S. Hayun, V. Paris, R. Mitrani, S. Kalabukhov, M. P. Dariel, E. Zaretsky, and N. Frage, "Microstructure and mechanical properties of silicon carbide processed by Spark Plasma Sintering (SPS)," *Ceram Int,* 38[8] 6335-40 (2012).

18. F. Guillard, A. Allemand, J. D. Lulewicz, and J. Galy, "Densitication of SiC by SPS-effects of time, temperature and pressure," *J Eur Ceram Soc,* 27[7] 2725-28 (2007).

19. S. J. Wu, L. C. DeJonghe, and M. N. Rahaman, "Sintering of nanophase gamma-Al2O3 powder," *J Am Ceram Soc,* 79[8] 2207-11 (1996).

20. E. A. Olevsky, S. Kandukuri, and L. Froyen, "Consolidation enhancement in spark-plasma sintering: Impact of high heating rates," *J Appl Phys,* 102[11] (2007).

21. E. Olevsky and L. Froyen, "Constitutive modeling of spark-plasma sintering of conductive materials," *Scripta Mater,* 55[12] 1175-78 (2006).

22. L. K. Mansur, A. F. Rowcliffe, R. K. Nanstad, S. J. Zinkle, W. R. Corwin, and R. E. Stoller, "Materials needs for fusion, Generation IV fission reactors and spallation neutron sources - similarities and differences," *J Nucl Mater,* 329 166-72 (2004).

23. S. J. Zinkle and J. T. Busby, "Structural materials for fission & fusion energy," *Mater Today,* 12[11] 12-19 (2009).

24. S. A. Maloy, M. Toloczko, J. Cole, and T. S. Byun, "Core materials development for the fuel cycle R&D program," *J Nucl Mater,* 415[3] 302-05 (2011).

25. M. J. Alinger, G. R. Odette, and D. T. Hoelzer, "On the role of alloy composition and processing parameters in nanocluster formation and dispersion strengthening in nanostuctured ferritic alloys," *Acta Mater,* 57[2] 392-406 (2009).

26. G. R. Odette, M. J. Alinger, and B. D. Wirth, "Recent developments in irradiation-resistant steels," *Annu Rev Mater Res,* 38 471-503 (2008).

27. J. Chen, P. Jung, W. Hoffelner, and H. Ullmaier, "Dislocation loops and bubbles in oxide dispersion strengthened ferritic steel after helium implantation under stress," *Acta Mater,* 56[2] 250-58 (2008).

28. A. Wasilkowska, M. Bartsch, U. Messerschmidt, R. Herzog, and A. Czyrska-Filemonowicz, "Creep mechanisms of ferritic oxide dispersion strengthened alloys," *J Mater Process Tech,* 133[1-2] 218-24 (2003).

29. M. B. Toloczko, D. S. Gelles, F. A. Garner, R. J. Kurtz, and K. Abe, "Irradiation creep and swelling from 400 to 600 degrees C of the oxide dispersion strengthened ferritic alloy MA957," *J Nucl Mater,* 329 352-55 (2004).

30. D. A. McClintock, D. T. Hoelzer, M. A. Sokolov, and R. K. Nanstad, "Mechanical properties of neutron irradiated nanostructured ferritic alloy 14YWT," *J Nucl Mater,* 386-88 307-11 (2009).

31. T. S. Byun, J. H. Kim, J. H. Yoon, and D. T. Hoelzer, "High temperature fracture characteristics of a nanostructured ferritic alloy (NFA)," *J Nucl Mater,* 407[2] 78-82 (2010).

32. K. Lu, "The future of metals," *Science,* 328[5976] 319-20 (2010).

33. T. Yano and B. Matovic, "Advanced Ceramics for Nuclear Applications," *Handbook of Advanced Ceramics: Materials, Applications, Processing, and Properties, 2nd Edition* 353-68 (2013).

34. M. K. Jain, J. Subrahmanyam, and S. Ray, "Development of Mo and Ta Foil Reinforced (MoSi2+20 vol% SiCp) Matrix Laminated Composites," *Adv Mater Res-Switz,* 585 306-10 (2012).

35. K. Debray, E. Martin, and J. M. Quenisset, "The effect of interfacial reactions on residual stress fields within composites," *J Compos Mater,* 33[4] 325-50 (1999).

36. R. C. J. Schiepers, F. J. J. Vanloo, and G. Dewith, "Reactions between Alpha-Silicon Carbide Ceramic and Nickel or Iron," *J Am Ceram Soc,* 71[6] C284-C87 (1988).

37. M. L. Hattali, S. Valette, F. Ropital, G. Stremsdoerfer, N. Mesrati, and D. Tréheux, "Study of SiC–nickel alloy bonding for high temperature applications," *J Eur Ceram Soc,* 29[4] 813-19 (2009).

38. J. Li, B. Y. Zong, Y. M. Wang, and W. B. Zhuang, "Experiment and modeling of mechanical properties on iron matrix composites reinforced by different types of ceramic particles," *Mat Sci Eng a-Struct,* 527[29-30] 7545-51 (2010).

39. J. Pelleg, "Reactions in the matrix and interface of the Fe-SiC metal matrix composite system," *Mat Sci Eng a-Struct,* 269[1-2] 225-41 (1999).

40. S. J. Zinkle, "Advanced materials for fusion technology," *Fusion Eng Des,* 74[1-4] 31-40 (2005).

41. S. J. Zinkle and G. S. Was, "Materials challenges in nuclear energy," *Acta Mater,* 61[3] 735-58 (2013).

42. S. J. Zinkle and J. T. Busby, "Structural materials for fission and fusion energy," *Mater Today,* 12[11] 12-19 (2009).

43. Z. A. Munir, U. Anselmi-Tamburini, and M. Ohyanagi, "The effect of electric field and pressure on the synthesis and consolidation of materials: A review of the spark plasma sintering method," *J Mater Sci,* 41[3] 763-77 (2006).

44. X. Y. Song, X. M. Liu, and J. X. Zhang, "Neck formation and self-adjusting mechanism of neck growth of conducting powders in spark plasma sintering," *J Am Ceram Soc,* 89[2] 494-500 (2006).

45. U. Anselmi-Tamburini, J. E. Garay, and Z. A. Munir, "Fundamental investigations on the spark plasma sintering/synthesis process III. Current effect on reactivity," *Mat Sci Eng a-Struct,* 407[1-2] 24-30 (2005).

46. U. Anselmi-Tamburini, J. E. Garay, Z. A. Munir, A. Tacca, F. Maglia, and G. Spinolo, "Spark plasma sintering and characterization of bulk nanostructured fully stabilized zirconia: Part I. Densification studies," *J Mater Res,* 19[11] 3255-62 (2004).

47. V. Mamedov, "Spark plasma sintering as advanced PM sintering method," *Powder Metall,* 45[4] 322-28 (2002).

48. Z. J. Shen, M. Johnsson, Z. Zhao, and M. Nygren, "Spark plasma sintering of alumina," *J Am Ceram Soc,* 85[8] 1921-27 (2002).

49. G. Skandan, H. Hahn, B. H. Kear, M. Roddy, and W. R. Cannon, "The Effect of Applied Stress on Densification of Nanostructured Zirconia during Sinter-Forging," *Mater Lett,* 20[5-6] 305-09 (1994).

50. J. Jamnik and R. Raj, "Space-charge-controlled diffusional creep: Volume diffusion case," *J Am Ceram Soc,* 79[1] 193-98 (1996).

51. Y. Zhou, K. Hirao, Y. Yamauchi, and S. Kanzaki, "Effects of heating rate and particle size on pulse electric current sintering of alumina," *Scripta Mater,* 48[12] 1631-36 (2003).

52. R. S. Dobedoe, G. D. West, and M. H. Lewis, "Spark plasma sintering of ceramics: understanding temperature distribution enables more realistic comparison with conventional processing," *Adv Appl Ceram,* 104[3] 110-16 (2005).

53. S. W. Wang, L. D. Chen, T. Hirai, and Y. S. Kang, "Microstructure inhomogeneity in Al2O3 sintered bodies formed during the plasma-activated sintering process," *J Mater Sci Lett,* 18[14] 1119-21 (1999).

54. M. Nygren and Z. J. Shen, "On the preparation of bio-, nano- and structural ceramics and composites by spark plasma sintering," *Solid State Sci,* 5[1] 125-31 (2003).

55. R. Naslain, "Design, preparation and properties of non-oxide CMCs for application in engines and nuclear reactors: an overview," *Compos Sci Technol,* 64[2] 155-70 (2004).

56. N. B. Morley, Y. Katoh, S. Malang, B. A. Pint, A. R. Raffray, S. Sharafat, S. Smolentsev, and G. E. Youngblood, "Recent research and development for the dual-coolant blanket concept in the US," *Fusion Eng Des,* 83[7-9] 920-27 (2008).

57. A. R. Raffray, R. Jones, G. Aiello, M. Billone, L. Giancarli, H. Golfier, A. Hasegawa, Y. Katoh, A. Kohyama, S. Nishio, B. Riccardi, and M. S. Tillack, "Design and material issues for high performance SiCf/SiC-based fusion power cores," *Fusion Eng Des,* 55[1] 55-95 (2001).

58. L. Charpentier, K. Dawi, M. Balat-Pichelin, E. Beche, and F. Audubert, "Chemical degradation of SiC/SiC composite for the cladding of gas-cooled fast reactor in case of severe accident scenarios," *Corros Sci,* 59 127-35 (2012).

59. K. Serivalsatit, B. Kokuoz, B. Yazgan-Kokuoz, M. Kennedy, and J. Ballato, "Synthesis, Processing, and Properties of Submicrometer-Grained Highly Transparent Yttria Ceramics," *J Am Ceram Soc,* 93[5] 1320-25 (2010).

60. K. J. Ning, J. Wang, D. W. Luo, J. Ma, J. Zhang, Z. L. Dong, L. B. Kong, and D. Y. Tang, "Fabrication and characterization of highly transparent Yb3+: Y2O3 ceramics," *Opt Mater,* 50 21-24 (2015).

61. I. Brooks, P. Lin, G. Palumbo, G. D. Hibbard, and U. Erb, "Analysis of hardness-tensile strength relationships for electroformed nanocrystalline materials," *Mat Sci Eng a-Struct,* 491[1-2] 412-19 (2008).

62. F. Khodabakhshi, M. Haghshenas, H. Eskandari, and B. Koohbor, "Hardness - strength relationships in fine and ultra-fine grained metals processed through constrained groove pressing," *Mat Sci Eng a-Struct,* 636 331-39 (2015).

63. I. A. Yakubtsov, P. Poruks, and J. D. Boyd, "Microstructure and mechanical properties of bainitic low carbon high strength plate steels," *Mat Sci Eng a-Struct,* 480[1-2] 109-16 (2008).

64. J. H. Yoon, Y. Lee, S. H. Kang, T. S. Byun, and D. T. Hoelzer, "Effects of Partial Phase Transformation on Characteristics of 9Cr Nanostructured Ferritic Alloy," *Curr Nanosci,* 10[1] 47-50 (2014).

65. J. Lacaze and B. Sundman, "An Assessment of the Fe-C-Si System," *Metall Trans A,* 22[10] 2211-23 (1991).

66. T. D. Shen, C. C. Koch, K. Y. Wang, M. X. Quan, and J. T. Wang, "Solid-state reaction in nanocrystalline Fe/SiC composites prepared by mechanical alloying," *J Mater Sci,* 32[14] 3835-39 (1997).

67. A. Bedolla-Jacuinde, W. Rainforth, and I. Mejia, "The Role of Silicon in the Solidification of High-Cr Cast Irons," *Metall Mater Trans A,* 44A[2] 856-72 (2013).

68. S. Kobayashi, K. Nakai, and Y. Ohmori, "Isothermal decomposition of delta-ferrite in a 25Cr-7Ni-0.14N stainless steel," *Acta Mater,* 49[11] 1891-902 (2001).

69. S. Kikuchi, Y. Nakahara, and J. Komotori, "Fatigue properties of gas nitrided austenitic stainless steel pre-treated with fine particle peening," *Int J Fatigue,* 32[2] 403-10 (2010).

70. J. A. Dean, "Lange's Handbook of Chemistry, 11th ed.″ McGRAW-HILL, INC.: New York, (1979).

71. D. R. Lide, "CRC Handbook, 84th ed.″ CRC Press: Boca Raton, Florida, (2003).

72. K. R. Gadelrab, G. Li, M. Chiesa, and T. Souier, "Local characterization of austenite and ferrite phases in duplex stainless steel using MFM and nanoindentation," *J Mater Res,* 27[12] 1573-79 (2012).

73. D. A. McClintock, M. A. Sokolov, D. T. Hoelzer, and R. K. Nanstad, "Mechanical properties of irradiated ODS-EUROFER and nanocluster strengthened 14YWT," *J Nucl Mater,* 392[2] 353-59 (2009).

74. A. Chauhan, D. Litvinov, and J. Aktaa, "High temperature tensile properties and fracture characteristics of bimodal 12Cr-ODS steel," *J Nucl Mater,* 468 1-8 (2016).

75. E. Gomez, J. Echeberria, I. Iturriza, and F. Castro, "Liquid phase sintering of SiC with additions of Y2O3, Al2O3 and SiO2," *J Eur Ceram Soc,* 24[9] 2895-903 (2004).

76. S. K. Bhaumik, C. Divakar, S. U. Devi, and A. K. Singh, "Synthesis and sintering of SiC under high pressure and high temperature," *J Mater Res,* 14[3] 906-11 (1999).

77. D. Sciti and A. Bellosi, "Effects of additives on densification, microstructure and properties of liquid-phase sintered silicon carbide," *J Mater Sci,* 35[15] 3849-55 (2000).

78. G. Magnani, G. Beltrami, G. L. Minoccari, and L. Pilotti, "Pressureless sintering and properties of alpha SiC-B4C composite," *J Eur Ceram Soc,* 21[5] 633-38 (2001).

79. P. Miao, G. R. Odette, T. Yamamoto, M. Alinger, D. Hoelzer, and D. Gragg, "Effects of consolidation temperature, strength and microstructure on fracture toughness of nanostructured ferritic alloys," *J Nucl Mater,* 367 208-12 (2007).

80. M. K. Miller, K. F. Russell, and D. T. Hoelzer, "Characterization of precipitates in MA/ODS ferritic alloys," *J Nucl Mater,* 351[1-3] 261-68 (2006).

81. K. Strecker, S. Ribeiro, R. Oberacker, and M. J. Hoffmann, "Influence of microstructural variation on fracture toughness of LPS-SiC ceramics," *Int J Refract Met H,* 22[4-5] 169-75 (2004).

82. T. Zhang, Z. Q. Zhang, J. X. Zhang, D. L. Jiang, and Q. L. Lin, "Preparation of SiC ceramics by aqueous gelcasting and pressureless sintering," *Mat Sci Eng a-Struct,* 443[1-2] 257-61 (2007).

83. P. G. Karandikar, G. Evans, S. Wong, M. K. Aghajanian, and M. Sennett, "A Review of Ceramics for Armor Applications," *Ceram Eng Sci Proc,* 29[6] 163-75 (2009).

84. G. Magnani, G. L. Minoccari, and L. Pilotti, "Flexural strength and toughness of liquid phase sintered silicon carbide," *Ceram Int,* 26[5] 495-500 (2000).

85. D. W. Shin, S. S. Park, Y. H. Choa, and K. Niihara, "Silicon/silicon carbide composites fabricated by infiltration of a silicon melt into charcoal," *J Am Ceram Soc,* 82[11] 3251-53 (1999).

86. S. H. Lee, Y. I. Lee, Y. W. Kim, R. J. Xie, M. Mitomo, and G. D. Zhan, "Mechanical properties of hot-forged silicon carbide ceramics," *Scripta Mater,* 52[2] 153-56 (2005).

87. X. F. Zhang, Q. Yang, and L. C. De Jonghe, "Microstructure development in hot-pressed silicon carbide: effects of aluminum, boron, and carbon additives," *Acta Mater,* 51[13] 3849-60 (2003).

88. Y. Zhou, K. Hirao, M. Toriyama, Y. Yamauchi, and S. Kanzaki, "Effects of intergranular phase chemistry on the microstructure and mechanical properties of silicon carbide

ceramics densified with rare-earth oxide and alumina additions," *J Am Ceram Soc,* 84[7] 1642-44 (2001).

89. D. F. Johnson and E. A. Carter, "Bonding and Adhesion at the SiC/Fe Interface," *J Phys Chem A,* 113[16] 4367-73 (2009).